

The DECADE cosmic shear project IV: cosmological constraints from 107 million galaxies across 5,400 deg² of the sky

D. Anbajagane (சுயிற)*^{1,2} C. Chang^{1,2} A. Drlica-Wagner^{3,1,2} C. Y. Tan^{4,2} M. Adamow^{5,6}
 R. A. Gruendl^{5,6} L. F. Secco² Z. Zhang^{1,7,8} M. R. Becker⁹ P. S. Ferguson¹⁰ N. Chicoine^{1,11}
 K. Herron¹² A. Alarcon¹³ R. Teixeira^{1,14} D. Suson¹⁵ A. N. Alsina¹⁶ A. Amon¹⁷ F. Andrade-Oliveira¹⁸
 J. Blazek¹⁹ C. R. Bom²⁰ H. Camacho²¹ J. A. Carballo-Bello²² A. Carnero Rosell^{23,24,25} R. Cawthon²⁶
 W. Cerny²⁷ A. Choi²⁸ Y. Choi²⁹ S. Dodelson^{2,3,1} C. Doux³⁰ K. Eckert³¹ J. Elvin-Poole³²
 J. Esteves³³ M. Gatti² G. Giannini² D. Gruen^{34,35} W. G. Hartley³⁶ K. Herner³ E. M. Huff³⁷
 D. J. James^{38,39} M. Jarvis³¹ E. Krause⁴⁰ N. Kuropatkin³ C. E. Martínez-Vázquez⁴¹ P. Massana⁴²
 S. Mau^{7,43} J. McCullough⁴⁴ G. E. Medina^{45,46} B. Mutlu-Pakdil¹² J. Myles¹⁷ M. Navabi⁴⁷
 N. E. D. Noël⁴⁷ A. B. Pace⁴⁸ A. Porredon⁴⁹ J. Prat⁵⁰ M. Raveri⁵¹ A. H. Riley⁵² E. S. Rykoff^{8,43}
 J. D. Sakowska⁴⁷ S. Samuroff⁵³ D. Sanchez-Cid^{54,18} D. J. Sand⁵⁵ L. Santana-Silva²⁰ I. Sevilla-Noarbe⁴⁹
 T. Shin⁵⁶ M. Soares-Santos¹⁸ G. S. Stringfellow⁵⁷ C. To² A. Tong³¹ M. A. Troxel¹⁴ A. K. Vivas⁵⁸
 M. Yamamoto¹⁷ B. Yanny⁵⁹ B. Yin¹⁴ Y. Zhang⁶⁰ and J. Zuntz⁶¹

¹ Department of Astronomy and Astrophysics, University of Chicago, Chicago, IL 60637, USA

² Kavli Institute for Cosmological Physics, University of Chicago, Chicago, IL 60637, USA

³ Fermi National Accelerator Laboratory, P. O. Box 500, Batavia, IL 60510, USA

⁴ Department of Physics, University of Chicago, Chicago, IL 60637, USA

⁵ Center for Astrophysical Surveys, National Center for Supercomputing Applications, 1205 West Clark St., Urbana, IL 61801, USA

⁶ Department of Astronomy, University of Illinois at Urbana-Champaign, 1002 W. Green Street, Urbana, IL 61801, USA

⁷ Department of Physics, Stanford University, 382 Via Pueblo Mall, Stanford, CA 94305, USA

⁸ SLAC National Accelerator Laboratory, Menlo Park, CA 94025, USA

⁹ Argonne National Laboratory, 9700 South Cass Avenue, Lemont, IL 60439, USA

¹⁰ DIRAC Institute, Department of Astronomy, University of Washington, 3910 15th Ave NE, Seattle, WA, 98195, USA

¹¹ Department of Physics and Astronomy, University of Pittsburgh, 3941 O'Hara Street, Pittsburgh, PA 15260

¹² Department of Physics and Astronomy, Dartmouth College, Hanover, NH 03755, USA

¹³ Institute of Space Sciences (ICE, CSIC), Campus UAB, Carrer de Can Magrans, s/n, 08193 Barcelona, Spain

¹⁴ Department of Physics, Duke University Durham, NC 27708, USA

¹⁵ Department of Chemistry and Physics, Purdue University Northwest 2200, 169th Ave, Hammond, IN 46323

¹⁶ Instituto de Física Gleb Wataghin, Universidade Estadual de Campinas, 13083-859, Campinas, SP, Brazil

¹⁷ Department of Astrophysical Sciences, Princeton University, Peyton Hall, Princeton, NJ 08544, USA

¹⁸ Physik-Institut, University of Zurich, Winterthurerstrasse 190, CH-8057 Zurich, Switzerland

¹⁹ Department of Physics, Northeastern University, Boston, MA 02115, USA

²⁰ Centro Brasileiro de Pesquisas Físicas, Rua Dr. Xavier Sigaud 150, 22290-180 Rio de Janeiro, RJ, Brazil

²¹ Physics Department, Brookhaven National Laboratory, Upton, NY 11973

²² Instituto de Alta Investigación, Universidad de Tarapacá, Casilla 7D, Arica, Chile

²³ Universidad de La Laguna, Dpto. Astrofísica, E-38206 La Laguna, Tenerife, Spain

²⁴ Instituto de Astrofísica de Canarias, E-38205 La Laguna, Tenerife, Spain

²⁵ Laboratório Interinstitucional de e-Astronomia - LIneA, Rua Gal. José Cristino 77, Rio de Janeiro, RJ - 20921-400, Brazil

²⁶ Physics Department, William Jewell College, Liberty, MO, 64068

²⁷ Department of Astronomy, Yale University, New Haven, CT 06520, USA

²⁸ NASA Goddard Space Flight Center, 8800 Greenbelt Rd, Greenbelt, MD 20771, USA

²⁹ NSF National Optical-Infrared Astronomy Research Laboratory, 950 North Cherry Avenue, Tucson, AZ 85719, USA

- ³⁰ *Université Grenoble Alpes, CNRS, LPSC-IN2P3, 38000 Grenoble, France*
- ³¹ *Department of Physics and Astronomy, University of Pennsylvania, Philadelphia, PA 19104, USA*
- ³² *Department of Physics and Astronomy, University of Waterloo, 200 University Ave W, Waterloo, ON N2L 3G1, Canada*
- ³³ *Department of Physics, Harvard University, MA 02138, USA*
- ³⁴ *University Observatory, Faculty of Physics, Ludwig-Maximilians-Universität, Scheinerstr. 1, 81679 Munich, Germany*
- ³⁵ *Excellence Cluster ORIGINS, Boltzmannstr. 2, 85748 Garching, Germany*
- ³⁶ *Department of Astronomy, University of Geneva, ch. d'Ecogia 16, 1290 Versoix, Switzerland*
- ³⁷ *Jet Propulsion Laboratory, California Institute of Technology, 4800 Oak Grove Dr., Pasadena, CA 91109, USA*
- ³⁸ *Applied Materials Inc., 35 Dory Road, Gloucester, MA 01930*
- ³⁹ *ASTRAVEO LLC, PO Box 1668, Gloucester, MA 01931*
- ⁴⁰ *Department of Astronomy/Steward Observatory, University of Arizona, Tucson, AZ 85721 USA*
- ⁴¹ *International Gemini Observatory/NSF NOIRLab, 670 N. A'ohoku Place, Hilo, Hawai'i, 96720, USA*
- ⁴² *NSF's NOIRLab, Casilla 603, La Serena, Chile*
- ⁴³ *Kavli Institute for Particle Astrophysics & Cosmology, P.O. Box 2450, Stanford University, Stanford, CA 94305, USA*
- ⁴⁴ *Department of Astrophysical Sciences, Peyton Hall, Princeton University, Princeton, NJ USA 08544*
- ⁴⁵ *Dunlap Institute for Astronomy & Astrophysics, University of Toronto, 50 St George Street, Toronto, ON M5S 3H4, Canada*
- ⁴⁶ *David A. Dunlap Department of Astronomy & Astrophysics, University of Toronto, 50 St George Street, Toronto ON M5S 3H4, Canada*
- ⁴⁷ *Department of Physics, University of Surrey, Guildford GU2 7XH, UK*
- ⁴⁸ *Department of Astronomy, University of Virginia, 530 McCormick Road, Charlottesville, VA 22904, USA*
- ⁴⁹ *Centro de Investigaciones Energéticas, Medioambientales y Tecnológicas (CIEMAT), Madrid, Spain*
- ⁵⁰ *Nordita, KTH Royal Institute of Technology and Stockholm University, SE-106 91 Stockholm.*
- ⁵¹ *Department of Physics and INFN, University of Genova, Genova, Italy*
- ⁵² *Institute for Computational Cosmology, Department of Physics, Durham University, South Road, Durham DH1 3LE, UK*
- ⁵³ *Institut de Física d'Altes Energies, The Barcelona Institute of Science and Technology, Campus UAB, 08193 Bellaterra (Barcelona) Spain*
- ⁵⁴ *Centro de Investigaciones Energéticas, Medioambientales y Tecnológicas (CIEMAT), Madrid, Spain*
- ⁵⁵ *Steward Observatory, University of Arizona, 933 North Cherry Avenue, Tucson, AZ 85721-0065, USA*
- ⁵⁶ *Department of Physics, Carnegie Mellon University, Pittsburgh, PA 15213*
- ⁵⁷ *Center for Astrophysics and Space Astronomy, University of Colorado, 389 UCB, Boulder, CO 80309-0389, USA*
- ⁵⁸ *Cerro Tololo Inter-American Observatory/NSF NOIRLab, Casilla 603, La Serena, Chile*
- ⁵⁹ *Fermi National Accelerator Laboratory, PO Box 500, Batavia, IL, 60510, USA*
- ⁶⁰ *NSF National Optical-Infrared Astronomy Research Laboratory, 950 N Cherry Avenue, Tucson, AZ 85719*
- ⁶¹ *Institute for Astronomy, University of Edinburgh, Edinburgh EH9 3HJ, UK*

Version February 26, 2025

ABSTRACT

We present cosmological constraints from the Dark Energy Camera All Data Everywhere (DECADE) cosmic shear analysis. This work uses shape measurements for 107 million galaxies measured through Dark Energy Camera (DECam) imaging of 5,412 deg² of sky that is outside the Dark Energy Survey (DES) footprint. We derive constraints on the cosmological parameters $S_8 = 0.791^{+0.027}_{-0.032}$ and $\Omega_m = 0.269^{+0.034}_{-0.050}$ for the Λ CDM model, which are consistent with those from other weak lensing surveys and from the cosmic microwave background. We combine our results with cosmic shear results from DES Y3 at the likelihood level, since the two datasets span independent areas on the sky. The combined measurements, which cover $\approx 10,000$ deg², prefer $S_8 = 0.791 \pm 0.023$ and $\Omega_m = 0.277^{+0.034}_{-0.046}$ under the Λ CDM model. These results are the culmination of a series of rigorous studies that characterize and validate the DECADE dataset and the associated analysis methodologies (Anbajagane et al. 2025a,b,c). Overall, the DECADE project demonstrates that the cosmic shear analysis methods employed in Stage-III weak lensing surveys can provide robust cosmological constraints for fairly inhomogeneous datasets. This opens the possibility of using data that have been previously categorized as “unusable” for cosmic shear analyses, thereby increasing the statistical power of upcoming weak lensing surveys.

1 INTRODUCTION

Observational cosmology is now a mature field with a multitude of distinct observational probes, each of which

provides unique insight into our understanding of the content and evolution of our Universe (e.g., Allen et al. 2011; Goobar & Leibundgut 2011; Mandelbaum 2018; Planck Collaboration et al. 2020b). Weak (gravitational) lensing is one mature cosmological probe that will be critical to further constrain the

*dhayaa@uchicago.edu, chihway@kip.uchicago.edu

physics of the low-redshift Universe (Spiegel et al. 2015; Racca et al. 2016; The LSST Dark Energy Science Collaboration et al. 2018) and also has the potential to improve our constraints on a wide variety of extended cosmological models such as modified gravity (e.g., Schmidt 2008), primordial signatures (e.g., Anbajagane et al. 2024c; Goldstein et al. 2024), etc.

Weak lensing is a phenomenon whereby light from distant sources is deflected by the presence of gravitational potentials — sourced by the matter distribution — present between the sources and the observer (Bartelmann & Schneider 2001; Schneider 2005). As a result, this phenomenon is sensitive to the distribution of all matter associated with this potential. Thus, weak lensing has long been regarded as an intrinsically clean cosmological probe that depends on only a few astrophysical processes, but is still sensitive to physics underlying the geometry of our Universe and to the growth of structure within it. A quarter-of-a-century after the first detection of this phenomenon (Bacon et al. 2000; Wittman et al. 2000; Kaiser et al. 2000), weak lensing has reached a state where the accuracy and robustness of the measurements (broadly categorized as systematics) are as important as the statistical precision of the probe (Asgari et al. 2021; Amon et al. 2022; Secco & Samuroff et al. 2022; Li et al. 2023). This is especially true given apparent discrepancies between cosmological constraints from weak lensing in galaxy surveys and the constraints inferred from the cosmic microwave background (CMB) (e.g., Asgari et al. 2021; Amon et al. 2022; Secco & Samuroff et al. 2022; Li et al. 2023; Planck Collaboration et al. 2020b). In particular, when assuming the Λ CDM model, weak lensing measurements prefer less structure in the matter distribution relative to the preference inferred from the CMB. This is usually referred to as the “ σ_8 tension” or “ S_8 tension”, where σ_8 is the normalization of the present-time, linear matter-power spectrum smoothed on $8h^{-1}\text{Mpc}$ scales, and $S_8 \equiv \sigma_8\sqrt{\Omega_m}/0.3$, where Ω_m is the ratio of the present-time matter energy density to the critical energy density.

In the context of these potential tensions, one of the most convincing cross-checks comes from performing independent analyses with different datasets, different algorithms, and preferably also different analysis teams. This is similar to the experimental design in high energy particle physics, where multiple groups — e.g., CMS (Chatrchyan et al. 2008) and ATLAS (Aad et al. 2008), or CDF (Abe et al. 1988) and DØ (Abachi et al. 1994) — analyze particle collider data in a fully independent, blinded fashion. Thus, if a discovery is confirmed by multiple groups, it is unlikely to be a systematic introduced by a specific experimental design. The large-scale structure community did not intentionally develop such structure, but one naturally emerged with the

three Stage-III¹ photometric galaxy surveys: the Dark Energy Survey (DES, Flaugher 2005), the Kilo-Degree Survey (KiDS, de Jong et al. 2015) and the Hyper Suprime-Cam Subaru Strategic Program (HSC-SSP, Aihara et al. 2018). To date, the headline weak lensing constraints from the three surveys give $S_8 = 0.759^{+0.025}_{-0.023}$ (DES, Secco & Samuroff et al. 2022; Amon et al. 2022), $S_8 = 0.759^{+0.024}_{-0.021}$ (KiDS, Asgari et al. 2021) and $S_8 = 0.769^{+0.031}_{-0.034}$ (HSC, Li et al. 2023). The combined, updated analysis of DES and KiDS Collaborations et al. (2023) gives $S_8 = 0.790^{+0.018}_{-0.014}$.

Interestingly, all these results find S_8 to be lower than the value inferred from the CMB ($S_8 = 0.832 \pm 0.013$, Planck Collaboration et al. 2020b). However, the regions of sky observed by three surveys partially overlap (see Figure 1), so the information is not entirely independent. The robustness of the S_8 tension could increase if statistically independent measurements corroborate the low S_8 value, and vice versa if independent measurements were to find no evidence of tension. This work presents the cosmological constraints from a fourth weak lensing dataset — the Dark Energy Camera All Data Everywhere (DECADE) — that has similar constraining power as the aforementioned Stage-III surveys and is statistically independent from the DES dataset.

This paper is part of a series of works in the DECADE cosmic shear project: Anbajagane & Chang et al. 2025a (hereafter PAPER I) describes the shape measurement pipeline, the derivation of the final source-galaxy sample for the weak lensing analysis, and the robustness tests and image simulation pipeline that characterize our measurements. Anbajagane et al. (2025b, hereafter PAPER II) derives the tomographic bins and calibrated redshift distributions for our source-galaxy sample, together with a series of validation tests. Anbajagane & Chang et al. 2025c (hereafter PAPER III) describes the methodology and validation of our cosmological inference pipeline, in addition to a series of tests to evaluate the impact of survey inhomogeneity. Lastly, this work (PAPER IV) shows our cosmic shear measurements and presents our constraints on parameters of different cosmological models.

The DECADE dataset is derived from multi-band Dark Energy Camera (DECam, Flaugher et al. 2015) imaging performed outside of the DES footprint. The catalog contains shape measurements for 107 million galaxies assembled from $5,412\text{ deg}^2$ of DECam imaging in the northern Galactic cap. The entire footprint is completely independent from DES. This dataset presents a unique opportunity to stress-test the S_8 tension in a number of ways. First, the DECADE multi-band coadded images were derived using the image processing

¹ The “Stage-X” terminology was introduced in Albrecht et al. (2006) to describe the different phases of dark energy experiments. There are currently four stages, where Stage-III refers to the dark energy experiments that started in the 2010s and Stage-IV refers to those that start in the 2020s.

pipeline used in the DES Year 6 campaign (Y6, [Bechtol et al. 2025](#)). Second, the DECADE source-galaxy catalog uses the METACALIBRATION measurement algorithm ([Sheldon & Huff 2017](#); [Huff & Mandelbaum 2017](#)) to estimate lensing shear from galaxies, and the self-organizing map photo-z (SOMPZ) method ([Buchs et al. 2019](#); [Myles & Alarcon et al. 2021](#); [Sánchez et al. 2023b](#)) to calibrate the galaxy redshift distributions; this follows the choices in DES Y3. However, in the process of executing the DECADE project, most parts of the analysis pipelines have been re-written and re-tested, confirming that the codes are robust.

Finally, the DECADE catalog effectively doubles the sky coverage of precision weak lensing datasets, and therefore improves the overlap between such weak lensing datasets and other wide-field cosmological surveys, including CMB experiments like Planck ([Planck Collaboration et al. 2020a](#)), the South Pole Telescope ([Carlstrom et al. 2011](#)), the Atacama Cosmology Telescope ([Fowler et al. 2007](#); [Thornton et al. 2016](#)), and the Simons Observatory ([Ade et al. 2019](#)); spectroscopic datasets such as the Sloan Digital Sky Survey ([York et al. 2000](#); [Dawson et al. 2013, 2016](#)) and the Dark Energy Spectroscopic Instrument ([DESI Collaboration et al. 2016](#)); as well as X-ray surveys like eROSITA ([Merloni et al. 2012](#)). Future work will perform cross-correlation analyses using the DECADE data to further stress-test the S_8 tension and to probe a variety of astrophysical and cosmological questions, as has already been pursued in the existing survey landscape (*e.g.*, [Shin et al. 2019](#); [Gatti et al. 2021](#); [Pandey et al. 2022](#); [Tröster et al. 2022](#); [Chang et al. 2023](#); [Omori et al. 2023](#); [Sánchez et al. 2023a](#); [Anbajagane et al. 2024b](#); [Bigwood et al. 2024](#)).

There is one more unique feature of the DECADE catalog that will be highlighted throughout this paper: the DECADE dataset was compiled from a collection of community-led DECam imaging campaigns and is significantly more inhomogeneous than the other Stage-III datasets mentioned above (*e.g.*, see Figure 12 in [PAPER I](#) or Figure 1 in [PAPER III](#)). Thus, the DECADE analysis stress-tests many of the shear algorithms and models in a regime where the data quality is more variable. While the next-generation of dedicated lensing surveys, such as the Vera C. Rubin Observatory Legacy Survey of Space and Time (LSST, [LSST Science Collaboration et al. 2009](#)), the *Nancy Grace Roman Space Telescope* ([Spergel et al. 2015](#)), and the Euclid mission ([Racca et al. 2016](#)), are expected to have a smaller level of inhomogeneity than that seen in the DECADE data, our findings still provide guidance on the level of variable data quality that can be accommodated in a lensing analysis. For example, the results of this work may motivate loosening data quality requirements when building a cosmology-ready sample, and thereby provide additional area/objects in the final sample of a given survey. This is especially relevant when considering the wide-fast-deep

footprint of LSST, which could be extended to higher/lower Galactic latitudes (*e.g.*, [Olsen et al. 2018](#)).

This work is structured as follows: in Section 2, we briefly describe the DECADE dataset, the cosmological model, and parameter inference pipeline we use. In Section 3, we summarize our blinding procedure, criteria for unblinding, and the results from the unblinding tests (a more detailed description is provided in Appendix C). The main results of this analysis are presented in Section 4, and we discuss our findings in Section 5. We conclude in Section 6. Additional analysis results are shown in Appendix A and B, and we will refer to them in the main text where relevant.

2 DATA, MODELING AND INFERENCE

We briefly summarize the DECADE dataset, our modeling choices, and our approach to parameter inference. For more technical details and discussion, we will direct the reader to results and discussions from the other papers in this series ([PAPER I](#), [PAPER II](#), [PAPER III](#)).

2.1 Data

The DECADE dataset is a galaxy shape catalog of 107 million galaxies spanning $5,412 \text{ deg}^2$ of the sky; see Figure 1 for the survey footprint compared to those of other surveys. The catalog is introduced in [PAPER I](#), alongside (i) a suite of null-tests that validate the absence of statistically significant systematics, and; (ii) an independent test/calibration of the measurement pipelines using an end-to-end image simulation campaign. The shear, $\gamma_{1,2}$, is estimated for each galaxy using the METACALIBRATION method ([Sheldon & Huff 2017](#); [Huff & Mandelbaum 2017](#)), with an approach designed to mimic that of DES Y3 ([Gatti & Sheldon et al. 2021](#); [MacCrann & Becker et al. 2022](#)). In [PAPER II](#), we split the shape catalog into four tomographic bins, and then estimate the redshift distribution of the ensemble in each bin using self-organizing maps (SOMPZ, [Buchs et al. 2019](#); [Myles & Alarcon et al. 2021](#)). We also cross-check these estimates using a spatial clustering-based approach ([Ménard et al. 2013](#); [Davis et al. 2017](#); [Gatti & Giannini et al. 2022](#)). Figure 2 shows the fiducial redshift distribution of our sample, as well as the distribution obtained from combining SOMPZ and the clustering-based approach.

The DECADE dataset is derived by combining available DECam community imaging data in the northern Galactic cap; see Figure 1 for the survey footprint. The nature of this dataset — as an amalgamation of available archival data, rather than as a dedicated weak lensing survey program — results in significant inhomogeneities in the survey observing conditions such as exposure time and image quality. This can propagate into variations in the observed (noisy) object

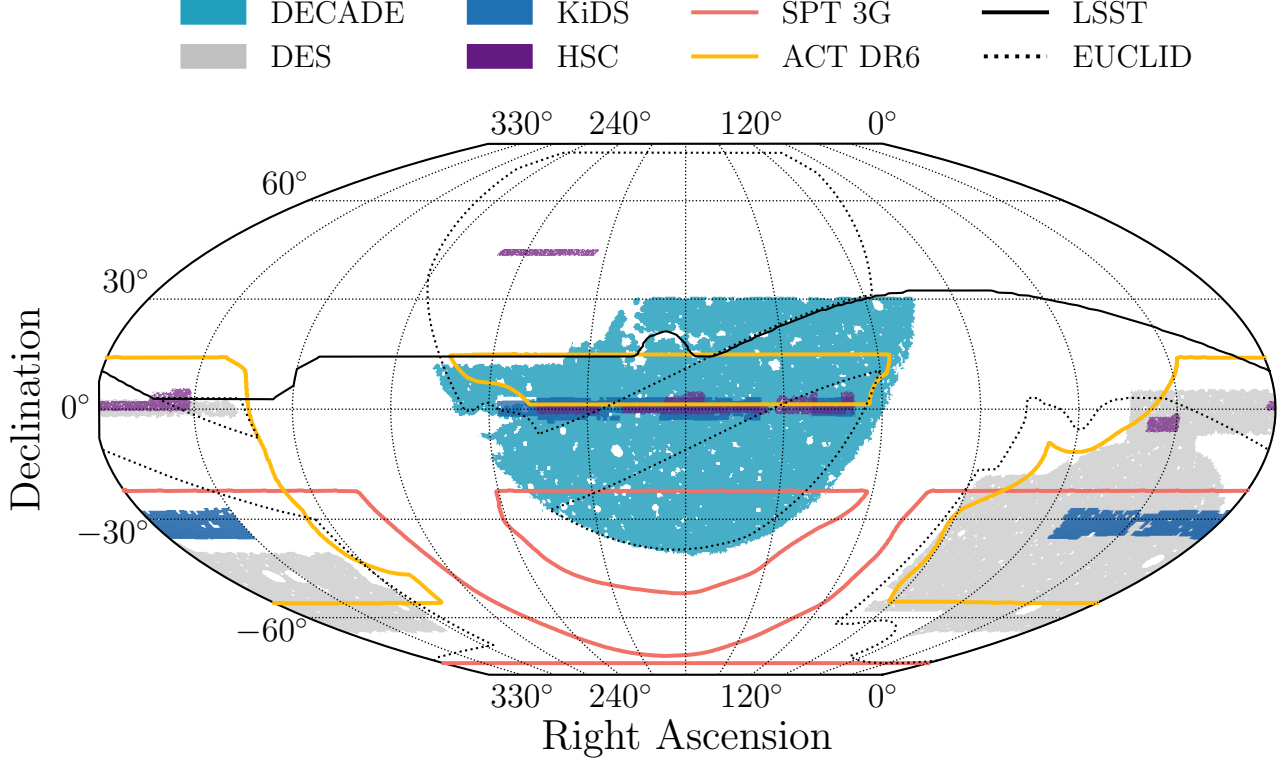


Figure 1. The footprint of the DECADE cosmic shear analysis, in relation to those of three other Stage-III surveys: DES Y3 (grey), KiDS-1000 (dark blue), and HSC Y3 (purple). We also show the footprints for the LSST wide-field survey, the *Euclid* wide-field survey, the SPT Ext-10k survey, and ACT DR6. See the introduction for references to the different experiments.

	n	$R_{\text{tot},1}$	$R_{\text{tot},2}$	$n_{\text{eff,H12}}$	$\sigma_{e,\text{H12}}$
Bin 1	1.396	0.836	0.837	1.239	0.233
Bin 2	1.371	0.771	0.771	1.150	0.259
Bin 3	1.375	0.740	0.742	1.169	0.248
Bin 4	1.369	0.620	0.621	1.153	0.289
Full sample	5.511	0.756	0.757	4.586	0.254

Table 1. The raw number density (n), different components of the shear response ($R_{\text{tot},1/2}$), effective number density of weak lensing galaxies (n_{eff}) and shape noise (σ_e) in the Heymans et al. (2006) definition, for each of the tomographic bins as well as the full non-tomographic sample. The number densities are calculated with an area of $5,412 \text{ deg}^2$, and are presented in units of arcmin^{-2} .

properties, and therefore the detection/selection functions of galaxy samples. While such inhomogeneities in observing conditions exist for other galaxy weak lensing surveys, such as DES, the amplitude of these variations are smaller than those found in the DECADE survey; see Figure 1 in PAPER III for a comparison. We have performed a variety of tests quantifying the impact of such inhomogeneity on cosmology constraints, and have found no evidence that these effects are larger than the current precision level of the data (see Section 6 of PAPER III). A summary of the dataset, including the source-galaxy number density and shape noise per tomographic bin, are found in Table 1 (reproduced from Table 2 of PAPER I).

Our fiducial cosmology constraints are derived from measurements of the shear two-point correlation functions. Following Bartelmann & Schneider (2001) and Schneider (2005)

$$\xi_{\pm} = \langle \gamma_t^a \gamma_t^b \rangle_{ab} \pm \langle \gamma_{\times}^a \gamma_{\times}^b \rangle_{ab}, \quad (1)$$

where the averages are taken over all galaxy pairs a, b , and $\gamma_t^{a,b}$ and $\gamma_{\times}^{a,b}$ are the tangential and cross components of the shear, as defined with respect to the line connecting galaxies a and b (e.g., see Equation 17 in Schneider 2005).

We do not have access to the shear field at the location of each galaxy, and therefore obtain it by averaging over the *ellipticities* of many galaxies. In practice, we estimate ξ_{\pm} as,

$$\xi_{\pm}^{ij}(\theta) = \frac{\sum_{ab} w_a w_b \left(\hat{e}_{t,a}^i \hat{e}_{t,b}^j \pm \hat{e}_{x,a}^i \hat{e}_{x,b}^j \right)}{\langle R \rangle_a \langle R \rangle_b \sum_{ab} w_a w_b}, \quad |\vec{\theta}_a - \vec{\theta}_b| \in \theta, \quad (2)$$

where i, j are indices over the four tomographic bins, \hat{e} are the mean-subtracted ellipticity estimates from METACALIBRATION, w are the (approximately) inverse-variance weights defined in PAPER I, and $\langle R \rangle$ is the weighted-average of the response measured from METACALIBRATION (see Table 1 and PAPER I for more details). The term $|\vec{\theta}_a - \vec{\theta}_b| \in \theta$ specifies that the sum \sum_{ab} is only over galaxy pairs with angular separations in the

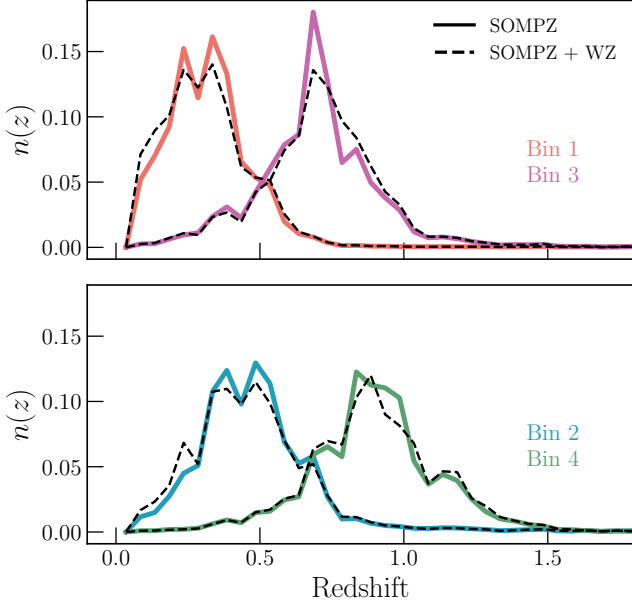


Figure 2. Redshift distribution for the four tomographic bins defined in the source-galaxy sample. We show both the fiducial redshift distributions derived from the SOMPZ method and also those from combining SOMPZ with information from the clustering redshift (WZ) method (see Section 3.7 of PAPER II).

angular bin θ . The measured data vector is shown in Figure 3, alongside the best-fit models derived from the analysis in Section 4.

There have also been extensive studies in the lensing community of alternative summary statistics beyond the two-point correlation functions, and the corresponding constraining power on the parameters of interest (*e.g.*, Jain et al. 1998; Friedrich et al. 2018; Gatti et al. 2022; Secco et al. 2022; Euclid Collaboration et al. 2023; Anbajagane et al. 2023; Gatti et al. 2024). While we follow the standard convention of the lensing community in this work and use the extensively tested two-point correlation functions as our measurement, we note that many works have performed robust lensing analyses using these alternative statistics (*e.g.*, Gruen et al. 2018; Zürcher et al. 2022; Fluri et al. 2022; Gatti et al. 2022, 2024; Jeffrey et al. 2025; Cheng et al. 2025). Such studies on the DECADE data will be pursued in the future.

2.2 Modeling and inference

A detailed description of our modeling choices are found in PAPER III. In brief, our modeling pipeline follows that of DES Y3 (Krause et al. 2021). The only difference is our choice to use HMCODE (Mead et al. 2020) as our model for the non-linear matter power spectrum, whereas DES Y3 used HALOFIT (Takahashi et al. 2012). The former has been shown to be more accurate than the latter (Mead et al. 2016, 2020,

2021) and was used in the DES & KiDS joint analysis (DES and KiDS Collaborations et al. 2023).

The two-point correlation functions can be modelled as,

$$\xi_{\pm}^{ij}(\theta) = \sum_{\ell} \frac{2\ell + 1}{2\pi\ell^2(\ell + 1)^2} [G_{\ell,2}^{+}(\cos\theta) \pm G_{\ell,2}^{-}(\cos\theta)] \times [C_{EE}^{ij}(\ell) \pm C_{BB}^{ij}(\ell)], \quad (3)$$

where the functions $G_{\ell}^{\pm}(x)$ are computed from Legendre polynomials $P_{\ell}(x)$ and averaged over angular bins (Krause et al. 2021). The i and j indices specify the two tomographic redshift bins from which the correlation function is calculated. The term C_{EE} is the matter power spectrum integrated along the line-of-sight after being weighted by the lensing kernels (see Equation 2 in PAPER III).

The intrinsic alignment (IA) of galaxies also contributes to the C_{EE} and C_{BB} terms. These are included in our predictions using the Tidally Aligned Tidally Torqued (TATT, Blazek et al. 2019) model, following Secco & Samuroff et al. (2022) and Amon et al. (2022). Similar to the latter two works, we also test a few variants for the IA model choice, including one with the simpler, non-linear alignment model (NLA, Bridle & King 2007) and one with no IA. The amplitude of the IA contribution is parameterized as,

$$A_1(z) = -a_1 \bar{C}_1 \frac{\rho_{\text{crit}} \Omega_m}{D(z)} \left(\frac{1+z}{1+z_0} \right)^{\eta_1}, \quad (4)$$

$$A_2(z) = 5a_2 \bar{C}_1 \frac{\rho_{\text{crit}} \Omega_m}{D^2(z)} \left(\frac{1+z}{1+z_0} \right)^{\eta_2}, \quad (5)$$

$$A_{1\delta}(z) = b_{\text{TA}} A_1(z), \quad (6)$$

where A_1 and A_2 scale the matter power spectra, $D(z)$ is the linear growth rate, ρ_{crit} is the critical density at $z = 0$, and $\bar{C}_1 = 5 \times 10^{-14} M_{\odot} h^{-2} \text{Mpc}^2$ is a normalization constant, set by convention. The free parameters of our model are the amplitudes a_1, a_2, b_{TA} and the power-law indices η_1, η_2 . The NLA model is obtained by setting $a_2, \eta_2, b_{\text{TA}} = 0$. See Equations 20–23 in Secco & Samuroff et al. (2022) for a description of the different IA-related power-spectra that contribute to the final signal.

As discussed in PAPER III, we fit the model above to our ξ_{\pm} measurements using a Markov Chain Monte Carlo (MCMC) approach. We assume a Gaussian likelihood L , with

$$\ln L(\xi_{\pm,d} | \mathbf{p}) = -\frac{1}{2} \left(\xi_{\pm,d} - \xi_{\pm,m}(\mathbf{p}) \right) \mathbf{C}^{-1} \left(\xi_{\pm,d} - \xi_{\pm,m}(\mathbf{p}) \right), \quad (7)$$

where ξ_{\pm} is a concatenation of the ξ_{+} and ξ_{-} measurements; $\xi_{\pm,d}$ and $\xi_{\pm,m}$ are the data vectors measured in the data and predicted from our theoretical model; \mathbf{C}^{-1} is the inverse covariance of the measurements; \mathbf{p} is a vector of the cosmology parameters and nuisance parameters listed in Table 2. The Bayesian posterior is proportional to the product of the

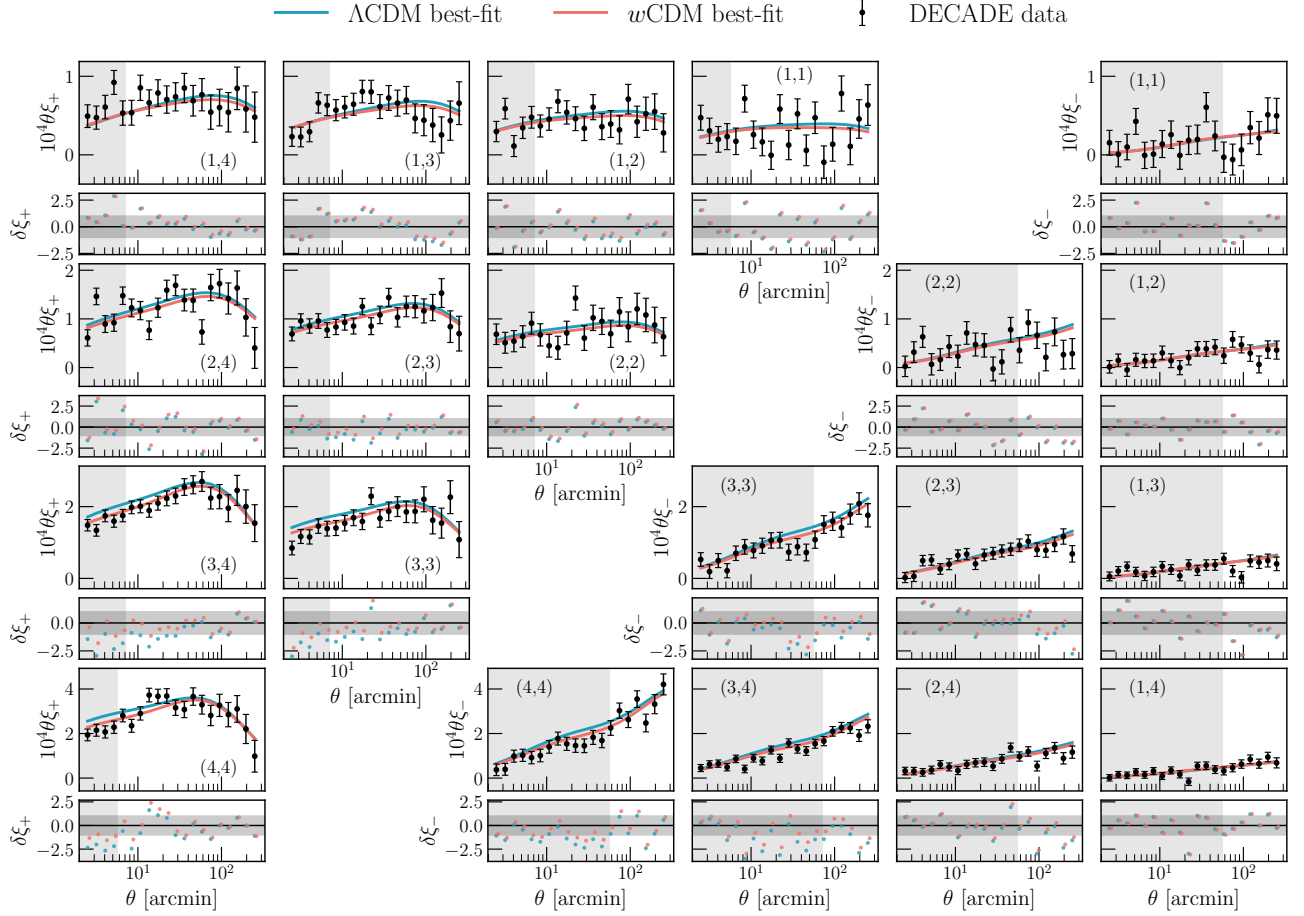


Figure 3. Our cosmic shear data vector and best-fit predictions under a Λ CDM and w CDM model. The upper (lower) triangle shows the ξ_+ (ξ_-) data vectors. Each panel corresponds to a bin pair, denoted in the legend. The shaded region marks angular scales removed during inference due to uncertainty in modeling baryonic effects. We show normalized residuals, $\delta\xi_{\pm} = (\xi_{\pm}^{\text{data}} - \xi_{\pm}^{\text{theory}})/\sigma_{\xi_{\pm}}$, in the lower sub-panel for each bin pair. The horizontal gray band covers the 1σ region around $\delta\xi_{\pm} = 0$.

likelihood L and the prior P , or

$$P(\mathbf{p}|\xi_{\pm,a}) \propto L(\xi_{\pm,a}|\mathbf{p})P(\mathbf{p}), \quad (8)$$

Table 2 lists the priors and fiducial values of all the model parameters. Our covariance matrix is generated using CosmoCov (Krause & Eifler 2017; Fang et al. 2020a,b) and follows the model of Friedrich et al. (2021) as used in DES Y3. This includes a simple Gaussian covariance, as well as a connected four-point term to account for non-linear structure (Wagner et al. 2015; Barreira & Schmidt 2017a,b), a super-sample contribution to incorporate correlations between small-scale modes as generated by modes larger than the survey footprint (e.g., Barreira et al. 2018), and also a correction for the impact of the survey mask on the shape noise term (Troxel et al. 2018).

All parameter inference is performed using the CosmoSIS package (Zuntz et al. 2015). We use Nautilus (Lange 2023) as the MCMC sampler for our fiducial chains, but we have checked that our results are consistent if we use the Polychord

sampler (Handley et al. 2015), which is the default choice in DES. The exact hyper-parameters used for the two samplers are listed in Table 2 of PAPER III.

Finally, in addition to our fiducial constraints, we also present joint constraints from DECADE and DES Y3. Given that the DECADE data comes from an independent patch of the sky relative to DES, there is negligible correlation between the two measurements and we can perform a joint analysis by simply multiplying the likelihoods from the two surveys. When doing so, there are two possible approaches for the IA model choices: first, we can use an independent set of parameters for each survey, resulting in 10 (4) free parameters under the TATT (NLA) model. Second, we can use a common set of parameters for both surveys, resulting in 5 (2) free parameters under the TATT (NLA) model. The latter choice is motivated by the fact that the galaxy selection (and detection) function is similar between DECADE and DES Y3 given the number of common choices across the image processing and catalog definition. We use the former, more

Parameter	Prior
Ω_m	$\mathcal{U}(0.1, 0.9)$
Ω_b	$\mathcal{U}(0.03, 0.07)$
h	$\mathcal{U}(0.55, 0.91)$
$A_s \times 10^9$	$\mathcal{U}(0.5, 5)$
n_s	$\mathcal{U}(0.87, 1.07)$
$\Omega_\nu h^2$	$\mathcal{U}(0.0006, 0.00644)$
a_1	$\mathcal{U}(-4, 4)$
a_2	$\mathcal{U}(-4, 4)$
η_1	$\mathcal{U}(-4, 4)$
η_2	$\mathcal{U}(-4, 4)$
b_{ta}	$\mathcal{U}(0, 2)$
Δz_1	$\mathcal{N}(0, 0.0163)$
Δz_2	$\mathcal{N}(0, 0.0139)$
Δz_3	$\mathcal{N}(0, 0.0101)$
Δz_4	$\mathcal{N}(0, 0.0117)$
m_1	$\mathcal{N}(-0.00923, 0.00296)$
m_2	$\mathcal{N}(-0.01895, 0.00421)$
m_3	$\mathcal{N}(-0.04004, 0.00428)$
m_4	$\mathcal{N}(-0.03733, 0.00462)$

Table 2. Cosmological and nuisance parameters in the baseline Λ CDM model. Uniform distributions in the range $[a, b]$ are denoted $\mathcal{U}(a, b)$ and Gaussian distributions with mean μ and standard deviation σ are denoted $\mathcal{N}(\mu, \sigma)$.

conservative choice for our fiducial analysis and present the latter in Appendix B1. We also use the fiducial scale cuts from DECADE and DES Y3 for this analysis, and have verified that the contamination from baryons causes a $< 0.3\sigma$ shift in the $\Omega_m - S_8$ plane of the joint analysis. Thus, the existing scale cuts pass the criteria defined by both DECADE (PAPER III) and DES Y3 (Secco & Samuroff et al. 2022; Amon et al. 2022).

3 BLINDING AND UNBLINDING

Modern cosmology analyses using galaxy surveys typically implement a *blinding* procedure (Heymans et al. 2021; DES Collaboration et al. 2022; Sugiyama et al. 2023), with the goal of preventing analysis choices from implicitly biasing the cosmological results. The purpose of blinding is to help the scientist perform all the necessary checks on the dataset and the analysis choices without knowing how these choices would impact the final result (the inferred cosmological parameter values, in our case). Different experiments have different approaches in blinding and unblinding. Overall, all Stage-III experiments have had fairly successful blinding experiences with minimal-to-no analysis changes made post-unblinding. This fact also makes the overall agreement between the different experiments’ constraints significant and highly non-trivial.

In this work, we apply blinding to our data vector according to the methodology described in Muir et al. (2020). In brief, we have a fiducial cosmology — that is a set of point values for the cosmological parameters — and an alternative one (chosen at random) that we use for blinding. We compute simulated data

vectors (ξ_\pm) for both cosmologies and find the shift induced by changing from one cosmology to another. This shift is then added to the measured data vector. In this work, our fiducial cosmology is given in Table 1 of PAPER III, and our alternative cosmology is given by taking the same and replacing the two parameters (σ_8, w) with random values drawn from a uniform distribution of $([0.714, 0.954], [-1.5, -0.5])$. Under this approach, our model will still be able to fit the blinded data vector with a reasonable χ^2 .

Note that our galaxy shape catalogs were not blinded, unlike what is done in DES Y3 and Y6 (Gatti & Sheldon et al. 2021; Yamamoto & Becker et al. 2025). Given the uniqueness of our dataset — and the potential oddities that could consequently arise and require detailed studies — we chose to keep the shape catalog unblinded so as to retain more flexibility in our analysis in the event of such scenarios. Furthermore, the catalog-level tests (those described in PAPER I) do not use/show measurements that are directly connected to the cosmological inference. In addition, the DECADE cosmology analysis team is small and the likelihood of accidentally unblinding ourselves (*e.g.*, by comparing our ξ_\pm data vector with DES) is low. Appendix C describes the full set of tests that we passed before unblinding.

4 RESULTS

This section presents all main results from the DECADE cosmic shear analysis. First, Figure 3 shows the measured data vectors in comparison with the best-fit Λ CDM and w CDM models. Both models are good descriptions of the data, with $\chi^2/N_{\text{data}} = 264.7/220$ (Λ CDM) and $\chi^2/N_{\text{data}} = 264.26/220$ (w CDM), where N_{data} is the number of data points. The effective number of constrained parameters² are 6.73 and 7.15 for the two models, which include 2.02 and 2.48 cosmological parameters, respectively.

We note that for the rest of this work we quote constraints from using the Nautilus sampler (Lange 2023), but we have checked that the numerical values we quote (mean, standard deviations, maximum-likelihood) are consistent with those estimated from Polychord (Handley et al. 2015), which is the standard sampler in DES Y3. Line 2 in Figure 6 below shows this comparison. We chose to use Nautilus because its importance sampling scheme requires significantly fewer likelihood evaluations to provide a converged chain.

Finally, all constraints quoted below show the mean and the 68% confidence interval, following DES Y3 (DES Collaboration et al. 2022). The confidence interval is computed using the 16% and 84% values of the distribution.

² Calculated via $N_{\text{eff}} \equiv N - \text{Tr}(C_{\Pi}^{-1} C_P)$, where N is the number of free parameters in the model, C_P is the posterior covariance and C_{Π} is the prior covariance.

All estimates of “distance” between two posteriors are calculated using a simple metric, using S_8 alone; see Equation C1. The posteriors in the cosmological parameters are always in good agreement with each other, and therefore we opt for this simpler estimator rather than the sophisticated metrics used in, for example, DES Y3 (Doux et al. 2021; Raveri & Doux 2021).

4.1 Λ CDM

We start by constraining the Λ CDM model. Figure 4 shows the posterior constraints for S_8 and Ω_m , while the posterior (and prior) of the full parameter space is shown in Appendix B3. Under a Λ CDM model, our constraints from DECADE are

$$S_8 = 0.791^{+0.027}_{-0.032} \quad (9)$$

$$\Omega_m = 0.269^{+0.034}_{-0.050}. \quad (10)$$

Figure 4 also overlays the constraints from DES Y3 obtained after re-analyzing the data vector using our inference pipeline. This differs from the analysis of Secco & Samuroff et al. (2022) and Amon et al. (2022) in not using information from DES shear ratios (Sánchez & Prat et al. 2022) and in switching to an updated model for the non-linear matter power spectrum; see Appendix A for details and comparison tests. We denote re-analyzed constraints with \star for clarity. The DECADE and DES Y3 data, both analyzed with our pipeline, are consistent at the 0.3σ level. We use Equation C1 to calculate these differences.

The same figure also shows constraints from *Planck* using their “TT+TE+EE+LowE” measurements (Planck Collaboration et al. 2020b). We extract the corresponding posteriors using the public *Planck* likelihood³ but using priors on cosmological parameters as shown in Table 2.⁴ The S_8 constraints from DECADE and *Planck* are consistent at the 1.1σ level. The constrained values of the cosmological parameters are listed in Table 3 below.

The results of Figure 4 show the S_8 constraint from DECADE has similar precision to that from the re-analyzed DES Y3 data, while the Ω_m constraint is notably more precise in the former compared to the latter. However, our simulated analysis finds the two surveys’ constraints have similar precision on Ω_m . The difference in the data constraints on Ω_m may be due to mild degeneracies between Ω_m and the IA amplitudes (a_1, a_2). This degeneracy is alleviated slightly in DECADE, relative to DES Y3, as the IA amplitudes of the former (particularly a_1) are well-constrained.

³ https://wiki.cosmos.esa.int/planck-legacy-archive/index.php/CMB_spectrum_%26_Likelihood_Code

⁴ In addition to the parameters in the table we also vary the optical depth τ with a uniform prior between 0.01 and 0.8.

4.1.1 Combined constraints from DECADE and DES Y3

The left panel of Figure 4 shows the combined constraints of DES Y3 and DECADE, obtained using the DECADE pipeline. We reiterate that the two surveys can be trivially combined because (1) the constraints are consistent with each other, and; (2) the datasets are entirely independent on the sky and so their measurements will have negligible cross-correlations. Therefore, the two surveys can be combined at the likelihood level. As a reminder (see Section 2.2 for more details), each dataset has its own set of shear calibration (m) and redshift calibration (Δz) parameters. While we perform two versions of the joint constraints — where the IA parameters are independent/shared for each dataset — we only show the constraint from the independent IA case and relegate the latter to Appendix B1. When using independent IA parameters, we find:

$$S_8 = 0.791 \pm 0.023 \quad (11)$$

$$\Omega_m = 0.277^{+0.034}_{-0.046} \quad (12)$$

The joint constraint on S_8 is consistent with that of *Planck* at the 1.2σ level.

The precision on S_8 after combining DECADE and DES Y3 is roughly 26% better than those of the individual surveys. Given the two weak lensing datasets have similar constraining power, the combination of the two can be expected to reduce statistical uncertainties (relative to the single-survey case) by a factor of $1/\sqrt{2} \approx 29\%$.⁵ Our simulated tests confirm the uncertainties on S_8 in the combined analysis are 29% smaller than those from the single-survey analyses. In practice, the DECADE constraint on S_8 is slightly better than that from DES Y3 (see Table 3). We therefore expect the improvement in the combined analysis to be slightly lower than our theoretical expectation, as is found in the case above.

Our combined constraints on S_8 are weaker than those from combining DES Y3 and KiDS-1000, quoted by DES and KiDS Collaborations et al. (2023) to be $S_8 = 0.790^{+0.018}_{-0.014}$. This is because the scale cuts used in our analysis are more conservative than those used in the latter work, and our choice of using the TATT IA model is also more flexible than the NLA model used in the latter work. Section 5.2 discusses the improvement in the DECADE-only constraints if we use the NLA model or use all scales in the analysis. Also, note that the Figure-of-Merit (FoM), defined in the $S_8 - \Omega_m$ plane and listed in Table 3, of the DECADE and DES Y3 \star combined analysis is only 12% lower than that of the DES Y3 and KiDS-1000 combined analysis.

⁵ We do not expect any degeneracy breaking — which would increase the expected improvement — when combining two similar datasets from the same cosmological probe.

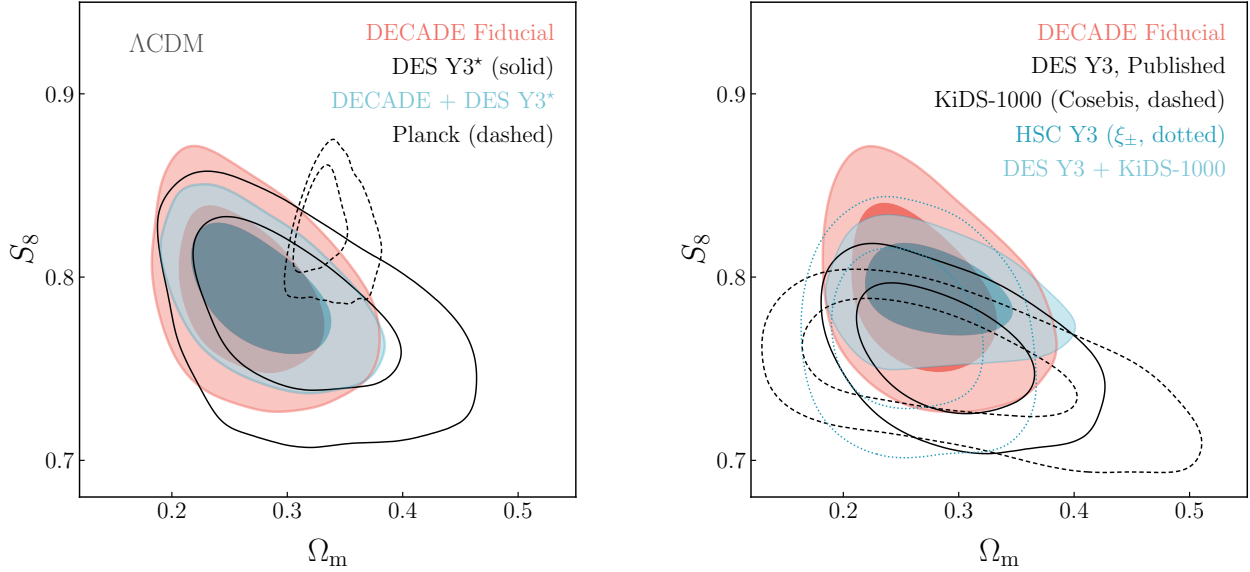


Figure 4. The fiducial Λ CDM cosmic shear constraints for Ω_m and S_8 . The \star denotes constraints re-analysed using our pipeline. All constraints are also listed in Table 3. **Left:** Results from DECADE (red), DES Y3 analyzed with our pipeline (black solid), the combination of the two (blue), and *Planck* (black dashed). The DECADE data constrains $S_8 = 0.791^{+0.027}_{-0.032}$, which is consistent with DES Y3 and also has similar constraining power to DES Y3 when both are analyzed with the same pipeline. The S_8 constraints from DECADE (DECADE + DES Y3) are consistent with *Planck* at the 1.1σ (1.2σ) level. **Right:** Comparison of the DECADE constraints with other published results. We do not reanalyze any data in this case and use the public posteriors. See Section 4.1.2 for references and links to the chains from the other lensing surveys.

4.1.2 Consistency with other cosmic shear surveys

In the right panel of Figure 4, we compare constraints from DECADE with other Stage-III cosmic shear surveys, as published by each of the collaborations. We do not reanalyze their data vectors with our own pipeline. Note that in this case, each survey makes assumptions and assigns priors (for both cosmology and nuisance parameters) that differ from those of the other surveys. While such choices do not change the qualitative findings of each survey, they still somewhat shift the exact constraints (*e.g.*, Chang et al. 2019; Longley et al. 2023; DES and KiDS Collaborations et al. 2023). With that caveat, we find that all of the recent cosmic shear constraints from Stage-III surveys are consistent with each other. We show results from DES Y3⁶ (Secco & Samuroff et al. 2022; Amon et al. 2022), KiDS-1000⁷ (Asgari et al. 2021), HSC Y3⁸ (Li et al. 2023; Dalal et al. 2023), and then the combination of the DES Y3 and KiDS-1000 data⁹ (DES and KiDS Collaborations et al. 2023). The KiDS-1000 analysis of Asgari et al. (2021) present constraints from analyzing multiple different data

⁶ https://desdr-server.ncsa.illinois.edu/despublic/y3a2_files/chains/chain_1x2pt_lcdm_SR_maglim.txt

⁷ https://kids.strw.leidenuniv.nl/DR4/data_files/KiDS1000_cosmic_shear_data_release.tgz

⁸ https://idark.ipmu.jp/~xiangchong.li/HSC/HSCY3/Li2023/hsc_y3_real_cosmic_shear.txt

⁹ https://desdr-server.ncsa.illinois.edu/despublic/y3a2_files/y3a2_joint-des-kids/chains/chain_desy3_and_kids1000_hybrid_analysis.txt

vector, and we show constraints from the COSEBI data vector, while HSC Y3 has a real-space (Li et al. 2023) and harmonic-space (Dalal et al. 2023) analysis, of which we show the former. The constraints from the companion analysis/data vectors that are omitted in Figure 4 are instead listed in Table 3.

4.2 wCDM

All constraints presented thus far are for a Λ CDM model of the Universe, *i.e.*, a model where dark energy has an equation of state $w = -1$. We now promote w to a free parameter of the model. This tests the evolution of the density of dark energy over time and can provide hints on the origin of the accelerated expansion of our Universe (*e.g.*, Mortonson et al. 2013; Linder 2023). This section presents the constraints for this model, w CDM.

Figure 5 shows the posterior constraints for Ω_m , S_8 and w . Our tests on simulated data vectors (performed post-unblinding) find that the w CDM constraints on S_8 and w incur some mild ($< 0.7\sigma$) projection effects on the mean value of the posterior.¹⁰ We stress that such effects do not indicate any bias in the posterior, but simply highlight the non-linear nature of the posteriors. All qualitative conclusions below, regarding the consistency between different results/constraints, are

¹⁰ For our Λ CDM analysis, we checked the impact of projections effects in PAPER III (see their Figure 2) and found it to be negligible in this case.

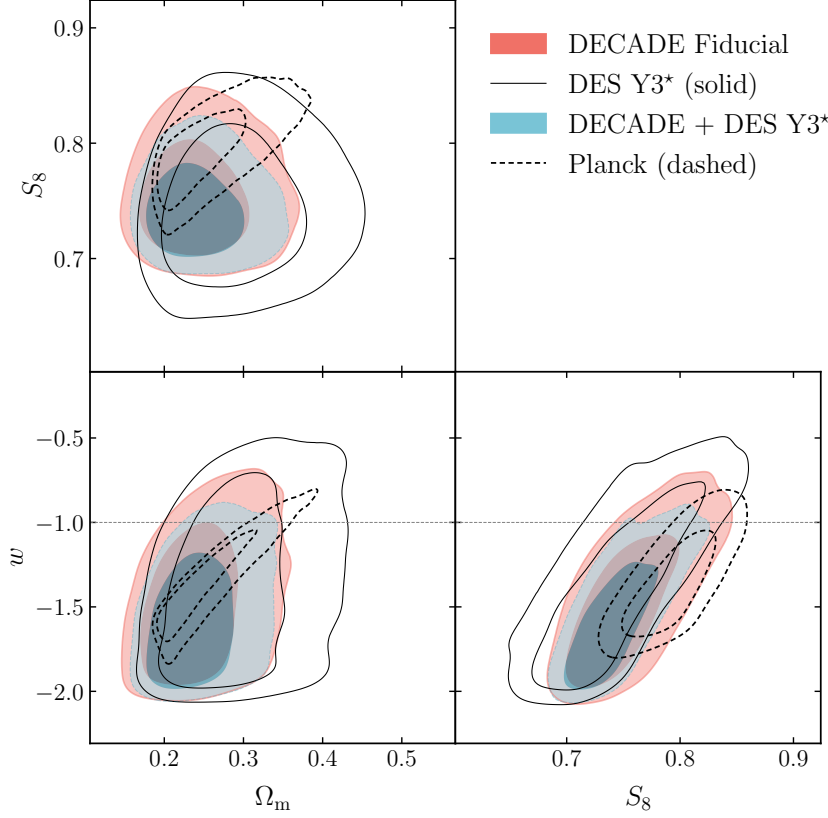


Figure 5. Cosmic shear constraints under a w CDM model, for Ω_m , S_8 and w . The constraint from DECADE (DECADE + DES Y3) is $w = -1.47^{+0.41}_{-0.25}$ ($w = -1.57^{+0.38}_{-0.16}$), which is consistent with *Planck* and with the Λ CDM expectation of $w = -1$ (dotted gray line). The DES Y3 data was re-analyzed using our pipeline. All presented constraints are listed in Table 3.

unchanged even under such effects. The DECADE constraints are,

$$S_8 = 0.753^{+0.024}_{-0.041}, \quad (13)$$

$$\Omega_m = 0.244^{+0.034}_{-0.057}, \quad (14)$$

$$w = -1.47^{+0.41}_{-0.25}. \quad (15)$$

The w CDM-based constraint on S_8 is shifted 1σ lower relative to the Λ CDM-based constraint, and this is consistent with the behavior found in DES Y3 (Secco & Samuroff et al. 2022, see Line 6 in their Figure 10). We note that the DES Y3 cosmic shear analysis does not quote a constraint on w (Secco & Samuroff et al. 2022; Amon et al. 2022) while the DECADE data has a weak constraint on the upper bound of w . Regardless, both results are consistent with $w = -1$; with the DECADE one being consistent at 1.3σ . The combined result

is similarly consistent with $w = -1$ at 1.5σ ,¹¹

$$S_8 = 0.743^{+0.020}_{-0.032}, \quad (16)$$

$$\Omega_m = 0.243^{+0.030}_{-0.049}, \quad (17)$$

$$w = -1.57^{+0.38}_{-0.16}. \quad (18)$$

The constraints are listed in Table 4. Additionally, Figure B2 below shows that the constraints on w are weakly correlated with a_2 , and that negative values of a_2 can slightly push w to more negative values.

5 DISCUSSION

To demonstrate the robustness of our cosmological constraints, we perform a number of additional tests on our analysis results. We summarize these in Figure 6 and Table

¹¹ In both cases, we use the upper-bound uncertainty as the σ in our distance metric (Equation C1). This is chosen because the point $w = -1$ is in the upper half of the posteriors.

Run	S_8	Ω_m	σ_8	w	χ^2/N_{data}	p	$\text{FoM}_{S_8\Omega_m}$
DECADE Fiducial	$0.791^{+0.026}_{-0.032}$	$0.268^{+0.033}_{-0.050}$	$0.845^{+0.075}_{-0.092}$	—	264.7/220	0.021	861
DES Y3*	0.779 ± 0.031	$0.307^{+0.043}_{-0.071}$	$0.782^{+0.086}_{-0.10}$	—	238.6/222	0.212	615
DECADE + DES Y3*	0.791 ± 0.023	$0.277^{+0.034}_{-0.046}$	$0.830^{+0.071}_{-0.082}$	—	502.0/442	0.025	1240
<i>Planck</i> 2018	0.827 ± 0.018	$0.332^{+0.010}_{-0.020}$	$0.786^{+0.030}_{-0.012}$	—	—	—	3252
DES Y3*, with SR	0.773 ± 0.026	$0.325^{+0.047}_{-0.069}$	$0.755^{+0.078}_{-0.098}$	—	241.0/222	0.182	847
DECADE + DES Y3*, with SR	0.787 ± 0.020	$0.295^{+0.036}_{-0.047}$	$0.801^{+0.065}_{-0.079}$	—	505.4/442	0.020	1522
DES Y3	0.759 ± 0.023	$0.290^{+0.041}_{-0.060}$	$0.783^{+0.075}_{-0.091}$	—	239.9/220	0.170	926
DES Y3, Λ CDM opt.	0.772 ± 0.017	$0.289^{+0.039}_{-0.054}$	0.795 ± 0.073	—	285.7/268	0.219	1362
KiDS-1000, COSEBIs	$0.751^{+0.024}_{-0.019}$	$0.286^{+0.056}_{-0.10}$	$0.79^{+0.12}_{-0.14}$	—	82.2/70	0.161	650
KiDS-1000, ξ_{\pm}	0.766 ± 0.018	$0.227^{+0.033}_{-0.053}$	0.894 ± 0.095	—	152.1/115	0.013	1165
KiDS-1000, bandpowers	$0.751^{+0.031}_{-0.022}$	$0.328^{+0.072}_{-0.10}$	$0.74^{+0.10}_{-0.14}$	—	260.3/220	0.034	588
HSC Y3, ξ_{\pm}	0.770 ± 0.030	$0.257^{+0.037}_{-0.050}$	$0.841^{+0.078}_{-0.087}$	—	150.0/140	0.266	786
HSC Y3, C_{ℓ}	0.778 ± 0.030	$0.225^{+0.027}_{-0.061}$	$0.914^{+0.11}_{-0.077}$	—	58.5/60	0.531	681
DES Y3 + KiDS-1000	$0.790^{+0.018}_{-0.016}$	$0.280^{+0.037}_{-0.047}$	0.825 ± 0.069	—	378.0/348	0.129	1415
DECADE, w CDM	$0.753^{+0.024}_{-0.041}$	$0.244^{+0.034}_{-0.057}$	0.848 ± 0.088	$-1.47^{+0.41}_{-0.25}$	264.3/220	0.022	611
DES Y3*, w CDM	$0.744^{+0.036}_{-0.054}$	$0.291^{+0.047}_{-0.073}$	$0.767^{+0.083}_{-0.099}$	$-1.38^{+0.58}_{-0.23}$	234.8/222	0.265	357
DECADE + Y3*, w CDM	$0.743^{+0.020}_{-0.032}$	$0.243^{+0.030}_{-0.049}$	0.835 ± 0.077	$-1.57^{+0.38}_{-0.16}$	504.1/442	0.022	851
<i>Planck</i> 2018, w CDM	$0.793^{+0.025}_{-0.028}$	$0.252^{+0.018}_{-0.056}$	$0.874^{+0.072}_{-0.042}$	$-1.37^{+0.26}_{-0.16}$	—	—	1126

Table 3. Summary of the constraints from our Λ CDM (top) and w CDM (bottom) analysis compared against other lensing results (middle). The constraints are shown in Figure 4 and 5. From left to right we list the constraints on cosmological parameters (S_8 , Ω_m , σ_8 , w), the reduced χ^2 of the best-fit cosmology, the associated p -value of that best-fit, and the figure of merit, $\text{FoM}_{S_8\Omega_m} = \det[\text{Cov}(S_8, \Omega_m)]^{-1/2}$. We use “DES Y3*” to denote the re-analysis of DES data using our pipeline (see Appendix A). All *Planck* constraints come from the “TT+TE+EE+LowE” dataset and use our priors for the cosmological parameters (see Section 4.1 for more details). We also compare against public results from DES Y3 (Secco & Samuroff et al. 2022; Amon et al. 2022), KiDS-1000 (Asgari et al. 2021), HSC Y3 (Li et al. 2023; Dalal et al. 2023) and the DES Y3 and KiDS-1000 joint analysis (DES and KiDS Collaborations et al. 2023). Our constraints on all cosmological parameters are in good agreement with other surveys, for both Λ CDM and w CDM. Amongst the public DES constraints shown in the middle rows, the combined analysis of DES Y3 and KiDS-1000 matches our choice in not using the DES shear ratio measurements (Sánchez & Prat et al. 2022), whereas the DES-only constraints do use this information.

4. We discuss below our interpretation of all these results. A subset of the tests mimic those we performed in PAPER III with simulated data vectors. A few of them are also connected to our pre-unblinding analysis and unblinding criteria, both of which are described in detail in Appendix C.

5.1 Goodness of fit

The two best-fit models shown in Figure 3 have a $\chi^2 \approx 264$ which, for $N_{\text{data}} = 220$, has a p -value corresponding to a 2σ discrepancy between data and model (see Table 3). While this passes our unblinding criteria (see Appendix C), the p -value is still somewhat on the lower side and motivated us to examine the fit in more depth.¹² We isolate the primary source of the high χ^2 to ξ_+ measurements in three, unrelated tomographic bin pairs: (1, 1), (2, 4), (4, 4). Discarding these bin pairs brings the p -value to under 1σ , but does not change our final cosmology constraint, *i.e.*, the measurements

¹² We also note that our p -value passes the criteria set by other surveys (Secco & Samuroff et al. 2022; Amon et al. 2022; Asgari et al. 2021) which varies between the thresholds $p > 0.001$ and $p > 0.01$.

contributing to the relatively high χ^2 of the total data vector do not push the cosmology constraints in a specific direction. The “oddity” in these bin pairs is their somewhat large, seemingly uncorrelated, scatter. To see if this large scatter correlates with image quality (or METACALIBRATION quantities), we visually checked data vectors from the forty-six subsets of the catalog analyzed in PAPER III but did not find any particular split that correlated with this larger scatter. Furthermore, when considering the goodness-of-fit for each of these forty-six splits, almost all splits have a χ^2 notably better than that found in our Fiducial case with the remaining splits exhibiting a χ^2 that is still similar or slightly better than that of the Fiducial case. Given these findings, we conclude that the origin of the scatter and the high χ^2 values is indeed from statistical fluctuations.

5.2 Intrinsic alignment

During the pre-unblinding analysis, we decided to use TATT as our fiducial IA model since using NLA resulted in a noticeably poorer goodness-of-fit. Furthermore, TATT

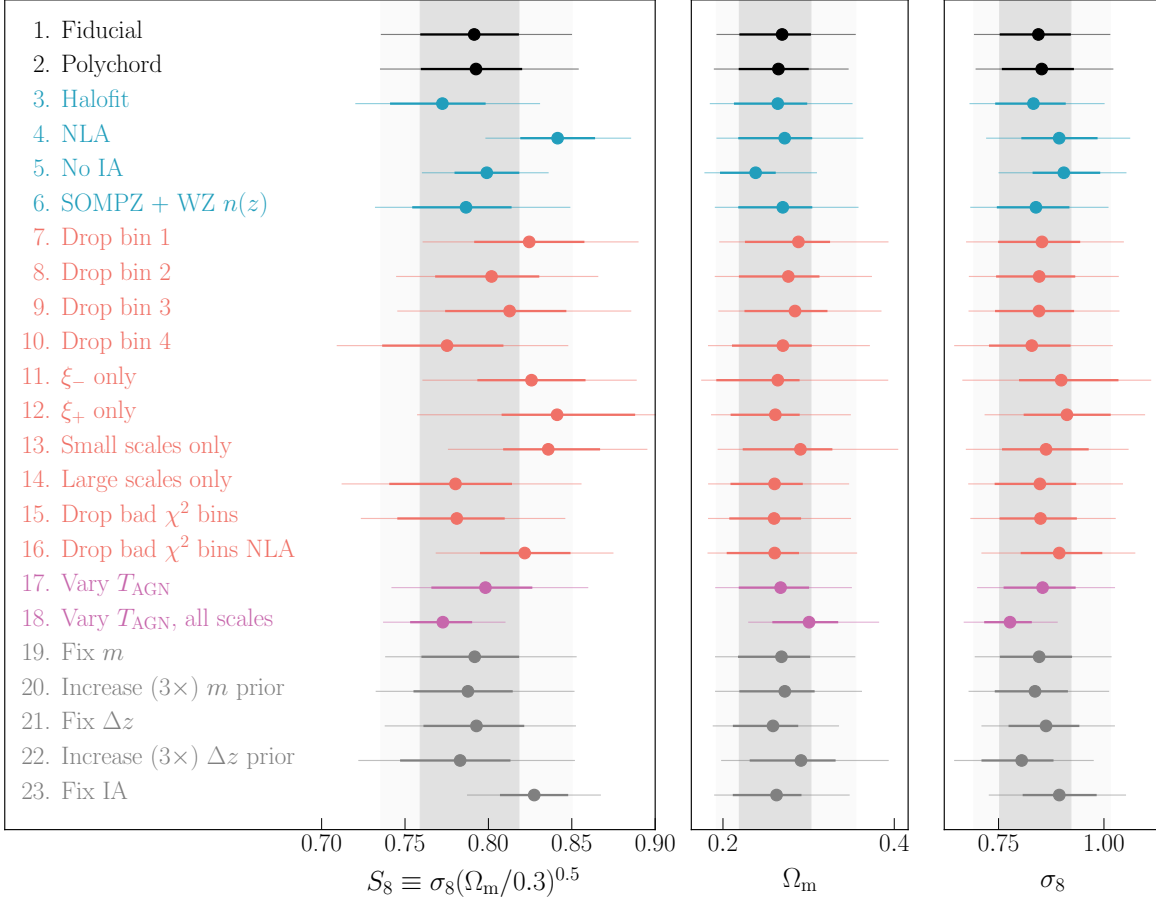


Figure 6. DECADE constraints in S_8 , Ω_m , and σ_8 for different variant analyses under our fiducial Λ CDM pipeline. The fiducial result is shown in line 1, and as a vertical gray band to facilitate comparison with other results. Line 2 shows our results are consistent across different samplers. Lines 3-6 considers alternative model assumptions. Lines 7-16 show constraints when only using part of our data vector. Lines 17-18 investigates changes to our result when we incorporate the small scales (which were previously discarded) and model baryonic corrections via an additional parameter (T_{AGN}). Lines 19-23 showcases the sensitivity of our constraints to our priors on the nuisance parameters. The detailed discussion of these points can be found in Section 5, while the numerical constraints are listed in Table 4.

reduces to the NLA model when fixing three of the five free parameters. After unblinding, we computed the Bayesian evidence ratios from the posteriors (*e.g.*, Secco & Samuroff et al. 2022, see their Equation 7) and find a clear preference in our data for TATT over NLA and over the “no IA” model. In particular NLA (no IA) is disfavored with a Bayesian evidence ratio of 0.013 (0.006) relative to the TATT model. This is consistent with our statement above that the goodness-of-fit improves considerably when using TATT over NLA. We note that the evidence ratios continue to favor TATT over NLA, with an evidence ratio of 0.042 for the latter, even if we drop the three bin pairs (see Section 5.1 above) that contribute most to degrading the goodness-of-fit. Thus, our data has a clear preference for the TATT model.

Our fiducial TATT constraints show the DECADE data

prefer a non-zero value for a_1 (a_2) at 2.8σ (2.9σ),

$$a_1 = 0.73^{+0.22}_{-0.46} \quad (19)$$

$$a_2 = -2.47^{+0.56}_{-0.65}. \quad (20)$$

There is no well-motivated prior expectation for the values of IA amplitudes (hence our wide prior) since the values depend on the exact galaxy sample being selected. However, our constraints on a_1 and a_2 are statistically consistent with the (broad) posteriors from DES Y3 (Secco & Samuroff et al. 2022; Amon et al. 2022) at 0.9σ and 1.5σ , respectively. Figure B1 shows this comparison in more detail.

The DECADE results find a statistically significant preference for non-zero IA amplitudes that is qualitatively consistent with other works (Samuroff et al. 2019; Asgari et al. 2021; DES and KiDS Collaborations et al. 2023); though, it is in contrast to the DES Y3 cosmic shear results (Secco & Samuroff et al. 2022; Amon et al. 2022), which

Run	S_8	Ω_m	$\chi^2/N_{\text{data}} (p)$
Fiducial	$0.791^{+0.027}_{-0.032}$	$0.269^{+0.034}_{-0.050}$	1.20 (0.021)
Polychord	$0.793^{+0.028}_{-0.033}$	$0.265^{+0.035}_{-0.046}$	1.21 (0.019)
Halofit	$0.772^{+0.026}_{-0.031}$	$0.264^{+0.034}_{-0.051}$	1.21 (0.019)
NLA	0.841 ± 0.022	$0.272^{+0.032}_{-0.054}$	1.29 (0.003)
No IA	0.799 ± 0.019	$0.238^{+0.023}_{-0.042}$	1.32 (0.001)
SOMPZ + WZ $n(z)$	$0.787^{+0.027}_{-0.032}$	$0.270^{+0.034}_{-0.052}$	1.21 (0.016)
Drop bin 1	0.824 ± 0.034	$0.288^{+0.037}_{-0.062}$	1.21 (0.051)
Drop bin 2	$0.802^{+0.029}_{-0.034}$	$0.276^{+0.036}_{-0.058}$	1.22 (0.046)
Drop bin 3	$0.813^{+0.034}_{-0.039}$	$0.284^{+0.038}_{-0.059}$	1.28 (0.016)
Drop bin 4	$0.775^{+0.034}_{-0.039}$	$0.270^{+0.034}_{-0.059}$	1.19 (0.066)
ξ_- only	0.826 ± 0.033	$0.264^{+0.025}_{-0.072}$	1.14 (0.203)
ξ_+ only	$0.841^{+0.047}_{-0.033}$	$0.261^{+0.028}_{-0.052}$	1.18 (0.060)
Small scales only	$0.836^{+0.031}_{-0.027}$	$0.290^{+0.037}_{-0.067}$	1.18 (0.090)
Large scales only	$0.780^{+0.034}_{-0.040}$	$0.260^{+0.033}_{-0.051}$	1.10 (0.228)
Drop bad χ^2 bins	$0.781^{+0.029}_{-0.036}$	$0.260^{+0.032}_{-0.052}$	0.98 (0.566)
Drop bad χ^2 bins NLA	0.822 ± 0.027	$0.260^{+0.028}_{-0.056}$	1.06 (0.290)
Vary T_{AGN}	$0.798^{+0.028}_{-0.032}$	$0.267^{+0.033}_{-0.049}$	1.19 (0.025)
Vary T_{AGN} , all scales	$0.773^{+0.018}_{-0.020}$	$0.301^{+0.034}_{-0.043}$	1.14 (0.031)
Fix m	$0.792^{+0.027}_{-0.032}$	$0.268^{+0.033}_{-0.051}$	1.20 (0.022)
Increase ($3\times$) m prior	$0.788^{+0.027}_{-0.033}$	$0.272^{+0.035}_{-0.053}$	1.20 (0.022)
Fix Δz	0.793 ± 0.030	$0.258^{+0.029}_{-0.047}$	1.23 (0.012)
Increase ($3\times$) Δz prior	$0.783^{+0.030}_{-0.036}$	$0.291^{+0.040}_{-0.060}$	1.19 (0.026)
Fix IA	0.827 ± 0.021	$0.263^{+0.029}_{-0.051}$	1.30 (0.002)

Table 4. The results from the various runs shown in Figure 6. From left to right, we list the run name, the constraints on S_8 and Ω_m , and the reduced χ^2 along with the associated p -value.

find no preference for an IA signal. It is possible that our constraint above reflects (at least partly) a real IA signal in the data. However, to be conservative, we posit other reasons our constraints may prefer non-zero values.

The IA parameter constraints can shift due to noisy data: Amon et al. (2022, see their Figure 15) show that noisy, simulated data vectors can generate posteriors that explore large values for a_1, a_2 . We have also verified this result through our own simulation tests. The IA parameters can also compensate for inaccurate estimates of the $n(z)$ distribution (*i.e.*, if the priors on the redshift calibrations are too narrow). Figure 6 shows a crude check of this effect, where broadening the redshift uncertainty by $3\times$ gives consistent constraints on S_8 . We have verified the IA constraints are similarly consistent if we broaden this prior.

To probe this further, we extract the contributions from the individual IA terms and show them in Figure B4. That figure, and the discussion surrounding it, finds that the preference for non-zero IA parameters originates from a slightly altered scale-dependence seen in the ξ_+ measurements (and somewhat from the ξ_- measurements as well), relative to a lensing-only

prediction. This trend is found in measurements across all bin pairs and changes mildly with redshift. We checked our data vector and IA constraints across the forty-six catalog-level splits in PAPER III, where the split is defined on image quality and object properties, and do not find any observational quantities that cause the preference for non-zero a_1, a_2 values. In fact, almost all of the forty-six splits also show a preference for $a_1 > 0$ and $a_2 < 0$, consistent with the Fiducial case. So, while our data prefers $a_1 > 0$ and $a_2 < 0$, the tests from PAPER III indicate this preference is not driven by a specific subset of the galaxies (*e.g.*, only those observed in particularly good/poor seeing or only those with small/large sizes).

Some of the variant runs in Figure 6 also show changes in their IA posteriors (see Figure B1); we discuss this further in Section 5.3. Specifically, they exhibit shifts to $a_2 \approx 0$. The a_1 posterior is relatively similar across the data vector-level splits shown in that figure and then η_2 , while still pushing against the upper bound of the prior, has a broader posterior that is now consistent with $\eta_2 = 0$. Removing subsets of the data vector causes a weakening in the previously mentioned trends with redshift and angular scales, which subsequently changes the IA posteriors. We explicitly show in Section 5.3 below that the S_8 constraints from these different variant analysis are all statistically consistent with each other. We direct the interested reader to Appendix B1 for a more extensive discussion on our IA results.

5.3 Constraints from subsets of the data vector: redshift bins, ξ_+ vs. ξ_- , large scale vs. small scale

An important validation of our final results is checking that different subsets of the data vector provide consistent constraints — *i.e.*, checking that the different subsets of the data vector are internally consistent with each other. We do this by dropping different parts of the data vector shown in Figure 3 and re-extracting our parameter constraints. Our tests are in Lines 7-16 (red) in Figure 6. We consider four such tests:

- drop one tomographic bin at a time, including all cross-correlations of that bin with others,¹³
- use only ξ_+ or ξ_- ,
- split the data vector (post scale-cuts) to use half of the smallest/largest scales in each bin-pair,
- Drop three bin pairs that contribute most to our relatively high χ^2 (see Section 5.1).

¹³ We also redid this analysis dropping the two lowest/highest redshift bins at once. However, in practice, this discards a majority of the data-vector and the resulting constraints on S_8 are consistent as the posteriors are significantly broader. The result of the test is therefore uninformative.

Dropping different tomographic bins changes the constraints by less than 1σ , as does dropping the three bin pairs that predominantly increase the χ^2 between the measurements and the best-fit model. Using only ξ_+ or ξ_- similarly changes the constraints by $\lesssim 1\sigma$.¹⁴ Finally, using only small-scales (large-scales) shifts the constraint by 1.07σ (0.28σ). Figure B1 shows the IA posteriors for a few variant analyses. The posteriors are broadly consistent with each other, though the constraint on a_2 is now broader and consistent with $a_2 = 0$.

We also note that three of the points (ξ_+ only, ξ_- only, and “Small scales” only) all shift to higher S_8 . Given we only have three points in this set, and all shifts are approximately within 1σ , the results are all still statistically consistent. Furthermore, analyzing noisy data with IA may cause seemingly correlated shifts. To explicitly test the significance of these shifts, we perform simulated tests of the exact analysis configuration, where we (i) generate a theoretical data vector at the best-fit value of the cosmology and nuisance parameters; (ii) add noise using the analytic covariance model, and; (iii) re-analyze the data vector under the ξ_+/ξ_- only and large/small-scale only analysis configuration. We run the four variant analyses on thirty noisy data vectors and extract S_8 in each case. We estimate the probability that our observed shifts in the four variant, “drop data” constraints are consistent with noise, and find $p \sim 0.1$. We obtain this by fitting a 4D multivariate Gaussian to the thirty best-fit values per analysis configuration, and finding the probability-to-exceed for the observed shifts. Other analysis choices — such as using kernel density estimators, incorporating the full posterior etc. — give probabilities that vary by $\Delta p \approx 0.05$. In the end, this is only a crude estimate of probability but shows that it is indeed possible for noise to generate the observed shifts.¹⁵

While we do not find any evidence that these shifts in the three points are systematics-driven rather than statistical fluctuations, we still briefly consider a thought experiment where the entire shift is due to systematics alone. Figure 6 shows the shift is at most $\lesssim 1\sigma$. Thus, even if the observed shifts in S_8 are completely systematics-driven, the shifts are still within the posterior of the Fiducial constraints. This last point is simply a restatement of our discussion above, that the three constraints are statistically consistent with the Fiducial one.

¹⁴ It may be surprising that the ξ_- constraining power is fairly similar to that of ξ_+ , even though the former has half as many datapoints after scale cuts. This is because both constraints are limited by uncertainties in the IA model, and the latter uncertainty is the same/similar across both analyses, resulting in similar posterior widths on S_8 . Similar behavior is found in the DES Y3 cosmic shear analysis (Amon et al. 2022, see their Figure 7)

¹⁵ We have also redone this exercise using a simulated data vector with the same best-fit cosmology but now removing the IA signal ($a_1 = a_2 = 0$). In this case, we find $p = 0.08$, which suggests that our probability estimate above is not that sensitive to our choice for the IA signal used in the simulated data vector.

5.4 Small-scale modeling

As discussed above, and also in PAPER III, a current limitation in weak-lensing analyses is uncertainty in the model for the small-scale power spectrum — particularly, for the signal of baryons on these scales. In our fiducial setup, we use the approach of DES Y3 (Secco & Samuroff et al. 2022; Amon et al. 2022) and remove scales where baryon corrections have a statistically noticeable impact on our data vector. In this section, we follow DES and KiDS Collaborations et al. (2023) in performing a variant analysis where we (i) use the same scale cuts as the Fiducial analysis but also marginalize over baryon corrections, and (ii) marginalize over baryon corrections but using all available datapoints, without imposing any scale cuts. We also follow that DES and KiDS Collaborations et al. (2023) in including the baryon corrections using the model of Mead et al. (2021). The corrections are parameterized by a single amplitude, T_{AGN} , which can be interpreted as an “effective feedback” parameter — larger values indicate stronger suppression of matter clustering. We use a prior of $T_{\text{AGN}} \in [10^{7.6}, 10^{8.0}]$, which is the range the model was calibrated to and is the same prior used in other works (DES and KiDS Collaborations et al. 2023; Bigwood et al. 2024).

Figure 6 shows the results for the marginal S_8 constraints while the posterior on other parameters are shown in Figure B5. In general, the constraints from these two variants are well within 1σ of our Fiducial constraint. The inclusion of a baryon component to our model does not change the goodness-of-fit by any appreciable amount, and does not change the IA constraints either. The shifts in S_8 , relative to the Fiducial constraints, are 0.15σ and 0.54σ when using/ignoring scale cuts, respectively.

5.5 Nuisance parameters

In line 19-23, we either reduce or increase the priors on the nuisance parameters and investigate the impact on the cosmological constraints. We note that the nuisance priors (m , Δz) are derived from PAPER I and PAPER II, respectively, and have been validated extensively. When changing the priors on these parameters to a delta function (line 19 and 21), we are checking how much a given nuisance parameter contributes to the final posterior width on S_8 . We find that for both m and Δz there is nearly no change in the S_8 constraints; this means our current uncertainties on m and Δz are not the limiting factors in the analysis. On the other hand, by increasing the prior width by $3\times$, we check the impact on cosmology if we incorrectly assumed overly tight priors. We find that for m the impact is still negligible. This is not surprising as our priors on m are quite small (relative to DES Y3) due to the larger number of image simulations we used (PAPER I). On the other hand, there is a small impact when we increase the Δz prior,

resulting in a degradation in S_8 by $\sim 10\%$. We also note that the mean value of S_8 shifts negligibly in the latter case.

We now move onto the IA parameters. If we fix the IA priors so that all the TATT parameters are delta functions, we find that the constraints on S_8 improve by nearly 30%. This makes explicit our previous statement that the final constraints are limited by uncertainties in the IA signals. The only difference between our “No IA” and “Fix IA” results is the former sets all IA amplitudes to zero whereas the latter sets them to the Fiducial values found in the DES 3×2 -point analysis (DES Collaboration et al. 2022); see Table 1 in PAPER III for the precise values. Both results show that the IA modeling is the limiting uncertainty in our analysis.

6 SUMMARY

In this paper, we present the cosmology results of the DECADE cosmic shear project. This work is the fourth in a series of papers detailing the rigorous testing, validation, and calibrations of the various data and modeling pipelines used for this project (PAPER I; PAPER II; PAPER III). The DECADE data is an amalgamation of over ten years of community-led observing with the Dark Energy Camera (DECam). The general-purpose catalog will be presented as part of Data Release 3 from the DECam Local Volume Exploration (DELVE) survey.

We have carried out a cosmic shear analysis with the DECADE data, closely following the methodologies of the DES Y3 cosmic shear pipeline. Our catalog contains 107 million galaxies across $5,412 \text{ deg}^2$ of the sky spanning the northern Galactic cap and is completely independent from the DES Y3 footprint. The data have a slightly lower source-galaxy number density relative to DES Y3 but covers a slightly larger area, and so have similar constraining power. Our fiducial cosmology constraint, under the Λ CDM model, is $S_8 = 0.791^{+0.026}_{-0.032}$ and $\Omega_m = 0.268^{+0.033}_{-0.050}$. The constraining power is similar to DES Y3 when both DECADE and DES Y3 are analyzed with the same pipeline.

Because the DECADE constraints are consistent with those of DES Y3, we are able to combine the two datasets. Furthermore, given they cover independent patches of the sky, we can perform the combination at the likelihood level. The combined cosmic shear analysis spans $\approx 10,000 \text{ deg}^2$, and gives Λ CDM constraints of $S_8 = 0.791 \pm 0.023$ and $\Omega_m = 0.277^{+0.034}_{-0.046}$. All constraints are consistent with previous lensing surveys as well as with the *Planck* 2018 constraints (Planck Collaboration et al. 2020b) from the CMB. When extending the model to w CDM, the DECADE data yield $w = -1.47^{+0.41}_{-0.25}$ while the combination of DECADE and DES Y3 gives $w = -1.57^{+0.38}_{-0.16}$. These are likewise consistent with constraints from *Planck* 2018 and with the Λ CDM expectation

of $w = -1$. The DECADE constraints (and the DECADE and DES Y3 combined constraints) are consistent with other lensing and CMB surveys to within 1σ to 1.5σ . All results, and their associated comparisons, are summarized in Table 3.

We have performed extensive tests on the internal consistency of the data vector, as well as of the constraints’ sensitivity to different modeling choices, and verified our constraints are robust. These are discussed in detail in Section 5 as well as the relevant appendices referred to therein. We also highlight our “split tests” in PAPER III, which involved splitting the dataset into subsets — based on sky location or some chosen object property — and re-running the entire end-to-end cosmic shear analysis pipeline (shear calibration, redshift estimation, covariance modeling etc.). We used forty-six different splits and found that all resulting constraints are consistent with the Fiducial constraint within 2σ . This is the first time these tests have been pursued at such scale in a cosmic shear analysis, and our work shows their utility in characterizing a wide range of systematics in lensing datasets.

As mentioned previously, the DECADE dataset is an amalgamation of many different community programs. This results in significantly larger variations in image quality (seeing, exposure time, depth, etc.) relative to other modern lensing surveys. These variations occur at the individual image-level and also across the sky. The DECADE project shows that a cosmic shear analysis with such a catalog, using established techniques from DES Y3, is still able to deliver robust constraints on S_8 at the 2 – 3% level. This work provides a reference point on the usability of imaging data that falls short of the “ideal” requirements for a weak lensing survey. Our results encourage exploring the construction of weak lensing datasets using imaging data from wider ranges of image quality/depth. Relaxing such criteria can significantly improve the size of the lensing dataset from a given survey, and therefore the precision of the survey as a whole. A salient, related point is that we find our constraints are limited dominantly by uncertainties in the IA modeling. This is similar to the findings from DES Y3 and further highlights the existing need, even in Stage-III surveys, for a better characterization of the IA signal.

Finally, we note that there is available DECam (community-derived) data in the *southern* Galactic cap, *surrounding* the DES footprint. These imaging data have been processed by DECADE, and the associated lensing catalogs, redshift distribution, calibrations, etc. will be generated. The cosmology constraints from this extended DECADE dataset will be presented in forthcoming work. Once completed, the full DECADE survey will fill-in much of the sky not covered by DES. Together the two surveys will enable a cosmology analysis spanning more than $13,000 \text{ deg}^2$, with coverage across most of the sky below $\text{Dec.} \lesssim 30^\circ$. This will provide the

community with an early preview of a Rubin LSST-esque dataset (though at shallower depth), which can be used to test techniques being developed for the Rubin LSST wide-field data and to also complement the many other experiments observing in this region of the sky that rely on optical/lensing data for their analyses/calibrations.

As we enter the next-generation of gravitational lensing experiments, the DECADE cosmic shear project showcases the full power and sophistication of one of the leading current-generation instruments, DECam. The continual use of DECam by the astronomical community and significant investments in its data processing pipelines have made DECam a vital tool in a wide variety of astronomical studies. Nearly two decades after it was first conceived, DECam has now imaged nearly three-fourths of the sky in multiple bands, and the combination of the DECADE and DES processing campaigns provide high-fidelity cosmic shear catalogs $> 10,000 \text{ deg}^2$ of the sky. This will serve as a useful legacy dataset as the next stage of cosmic shear experiments commence.

ACKNOWLEDGEMENTS

DA is supported by the National Science Foundation (NSF) Graduate Research Fellowship under Grant No. DGE 1746045. CC is supported by the Henry Luce Foundation and Department of Energy (DOE) grant DE-SC0021949. The DECADE project is supported by NSF AST-2108168 and AST-2108169. The DELVE Survey gratefully acknowledges support from Fermilab LDRD (L2019.011), the NASA *Fermi* Guest Investigator Program Cycle 9 (No. 91201), and the NSF (AST-2108168, AST-2108169, AST-2307126, AST-2407526, AST-2407527, AST-2407528). This work was completed in part with resources provided by the University of Chicago's Research Computing Center. The project that gave rise to these results received the support of a fellowship from "la Caixa" Foundation (ID 100010434). The fellowship code is LCF/BQ/PI23/11970028. C.E.M.-V. is supported by the international Gemini Observatory, a program of NSF NOIRLab, which is managed by the Association of Universities for Research in Astronomy (AURA) under a cooperative agreement with the U.S. National Science Foundation, on behalf of the Gemini partnership of Argentina, Brazil, Canada, Chile, the Republic of Korea, and the United States of America.

Funding for the DES Projects has been provided by the U.S. Department of Energy, the U.S. National Science Foundation, the Ministry of Science and Education of Spain, the Science and Technology Facilities Council of the United Kingdom, the Higher Education Funding Council for England, the National Center for Supercomputing Applications at the University of Illinois at Urbana-Champaign, the Kavli Institute of Cosmological Physics at the University of Chicago, the Center

for Cosmology and Astro-Particle Physics at the Ohio State University, the Mitchell Institute for Fundamental Physics and Astronomy at Texas A&M University, Financiadora de Estudos e Projetos, Fundação Carlos Chagas Filho de Amparo à Pesquisa do Estado do Rio de Janeiro, Conselho Nacional de Desenvolvimento Científico e Tecnológico and the Ministério da Ciência, Tecnologia e Inovação, the Deutsche Forschungsgemeinschaft and the Collaborating Institutions in the Dark Energy Survey.

The Collaborating Institutions are Argonne National Laboratory, the University of California at Santa Cruz, the University of Cambridge, Centro de Investigaciones Energéticas, Medioambientales y Tecnológicas-Madrid, the University of Chicago, University College London, the DES-Brazil Consortium, the University of Edinburgh, the Eidgenössische Technische Hochschule (ETH) Zürich, Fermi National Accelerator Laboratory, the University of Illinois at Urbana-Champaign, the Institut de Ciències de l'Espai (IEEC/CSIC), the Institut de Física d'Altes Energies, Lawrence Berkeley National Laboratory, the Ludwig-Maximilians Universität München and the associated Excellence Cluster Universe, the University of Michigan, NSF's NOIRLab, the University of Nottingham, The Ohio State University, the University of Pennsylvania, the University of Portsmouth, SLAC National Accelerator Laboratory, Stanford University, the University of Sussex, Texas A&M University, and the OzDES Membership Consortium.

The DES data management system is supported by the National Science Foundation under Grant Numbers AST-1138766 and AST-1536171. The DES participants from Spanish institutions are partially supported by MICINN under grants ESP2017-89838, PGC2018-094773, PGC2018-102021, SEV-2016-0588, SEV-2016-0597, and MDM-2015-0509, some of which include ERDF funds from the European Union. IFAE is partially funded by the CERCA program of the Generalitat de Catalunya. Research leading to these results has received funding from the European Research Council under the European Union's Seventh Framework Program (FP7/2007-2013) including ERC grant agreements 240672, 291329, and 306478. We acknowledge support from the Brazilian Instituto Nacional de Ciência e Tecnologia (INCT) do e-Universo (CNPq grant 465376/2014-2).

Based in part on observations at Cerro Tololo Inter-American Observatory at NSF's NOIRLab, which is managed by the Association of Universities for Research in Astronomy (AURA) under a cooperative agreement with the National Science Foundation.

This work has made use of data from the European Space Agency (ESA) mission *Gaia* (<https://www.cosmos.esa.int/gaia>), processed by the *Gaia* Data Processing and

Analysis Consortium (DPAC, <https://www.cosmos.esa.int/web/gaia/dpac/consortium>). Funding for the DPAC has been provided by national institutions, in particular the institutions participating in the *Gaia* Multilateral Agreement.

This paper is based on data collected at the Subaru Telescope and retrieved from the HSC data archive system, which is operated by the Subaru Telescope and Astronomy Data Center (ADC) at NAOJ. Data analysis was in part carried out with the cooperation of Center for Computational Astrophysics (CfCA), NAOJ. We are honored and grateful for the opportunity of observing the Universe from Maunakea, which has the cultural, historical and natural significance in Hawaii.

This manuscript has been authored by Fermi Forward Discovery Group, LLC under Contract No. 89243024CSC000002 with the U.S. Department of Energy, Office of Science, Office of High Energy Physics.

All analysis in this work was enabled greatly by the following software: PANDAS (McKinney 2011), NUMPY (Van der Walt et al. 2011), SCIPY (Virtanen et al. 2020), and MATPLOTLIB (Hunter 2007). We have also used the Astrophysics Data Service (ADS) and arXiv preprint repository extensively during this project and the writing of the paper.

DATA AVAILABILITY

All catalogs and derived data products (data vectors, redshift distributions, calibrations etc.) will be made public upon acceptance of the cosmology results.

REFERENCES

- Aad G., et al., 2008, *JINST*, 3, S08003
- Abachi S., et al., 1994, *Nucl. Instrum. Meth. A*, 338, 185
- Abe F., et al., 1988, *Nucl. Instrum. Meth. A*, 271, 387
- Ade P., et al., 2019, *J. Cosmology Astropart. Phys.*, 2019, 056
- Aihara H., et al., 2018, *PASJ*, 70, S4
- Albrecht A., et al., 2006, *arXiv e-prints*, pp astro-ph/0609591
- Allen S. W., Evrard A. E., Mantz A. B., 2011, *ARA&A*, 49, 409
- Amon A., Efstathiou G., 2022, *MNRAS*, 516, 5355
- Amon A., et al., 2022, *Phys. Rev. D*, 105, arXiv:2105.13543
- Anbajagane D., Evrard A. E., Farahi A., Barnes D. J., Dolag K., McCarthy I. G., Nelson D., Pillepich A., 2020, *MNRAS*, 495, 686
- Anbajagane D., Evrard A. E., Farahi A., 2022a, *MNRAS*, 509, 3441
- Anbajagane D., et al., 2022b, *MNRAS*, 510, 2980
- Anbajagane D., et al., 2023, *MNRAS*, 526, 5530
- Anbajagane D., Pandey S., Chang C., 2024a, *arXiv e-prints*, p. arXiv:2409.03822
- Anbajagane D., et al., 2024b, *MNRAS*, 527, 9378
- Anbajagane D., Chang C., Lee H., Gatti M., 2024c, *J. Cosmology Astropart. Phys.*, 2024, 062
- Anbajagane D., et al., 2025c
- Anbajagane D., et al., 2025b
- Anbajagane D., et al., 2025a
- Aricò G., Angulo R. E., Contreras S., Ondaro-Mallea L., Pellejero-Ibañez M., Zennaro M., 2021, *MNRAS*, 506, 4070
- Asgari M., et al., 2021, *A&A*, 645, A104
- Bacon D. J., Refregier A. R., Ellis R. S., 2000, *MNRAS*, 318, 625
- Barreira A., Schmidt F., 2017a, *J. Cosmology Astropart. Phys.*, 2017, 053
- Barreira A., Schmidt F., 2017b, *J. Cosmology Astropart. Phys.*, 2017, 051
- Barreira A., Krause E., Schmidt F., 2018, *J. Cosmology Astropart. Phys.*, 2018, 015
- Bartelmann M., Schneider P., 2001, *Phys. Rep.*, 340, 291
- Bechtol K., et al., 2025, *arXiv e-prints*, p. arXiv:2501.05739
- Bigwood L., et al., 2024, *arXiv e-prints*, p. arXiv:2404.06098
- Blazek J. A., MacCrann N., Troxel M. A., Fang X., 2019, *Phys. Rev. D*, 100, 103506
- Bridle S., King L., 2007, *New Journal of Physics*, 9, 444
- Buchs R., et al., 2019, *MNRAS*, 489, 820
- Carlstrom J. E., et al., 2011, *PASP*, 123, 568
- Chang C., et al., 2019, *MNRAS*, 482, 3696
- Chang C., et al., 2023, *Phys. Rev. D*, 107, 023530
- Chatrchyan S., et al., 2008, *JINST*, 3, S08004
- Cheng S., Marques G. A., Grandón D., Thiele L., Shirasaki M., Ménard B., Liu J., 2025, *J. Cosmology Astropart. Phys.*, 2025, 006
- Chisari N. E., et al., 2018, *MNRAS*, 480, 3962
- DES Collaboration Abbott T. M. C., et al., 2022, *Phys. Rev. D*, 105, 023520
- DES and KiDS Collaborations et al., 2023, *The Open Journal of Astrophysics*, 6, 36
- DESI Collaboration et al., 2016, *arXiv e-prints*, p. arXiv:1611.00036
- Dalal R., et al., 2023, *Phys. Rev. D*, 108, 123519
- Davis C., et al., 2017, *arXiv e-prints*, p. arXiv:1710.02517
- Dawson K. S., et al., 2013, *The Astronomical Journal*, 145, 10
- Dawson K. S., et al., 2016, *The Astronomical Journal*, 151, 44
- Doux C., et al., 2021, *MNRAS*, 503, 2688
- Euclid Collaboration et al., 2023, *A&A*, 675, A120
- Fang X., Krause E., Eifler T., 2020a, CosmoCov: Configuration space covariances for projected galaxy 2-point statistics, *Astrophysics Source Code Library*, record ascl:2006.005
- Fang X., Eifler T., Krause E., 2020b, *MNRAS*, 497, 2699
- Flaugher B., 2005, *International Journal of Modern Physics A*, 20, 3121
- Flaugher B., et al., 2015, *The Astronomical Journal*, 150, 150
- Fluri J., Kacprzak T., Lucchi A., Schneider A., Refregier A., Hofmann T., 2022, *Phys. Rev. D*, 105, 083518
- Fowler J. W., et al., 2007, *Appl. Opt.*, 46, 3444
- Friedrich O., et al., 2018, *Phys. Rev. D*, 98, 023508
- Friedrich O., et al., 2021, *MNRAS*, 508, 3125
- Gatti & Giannini et al., 2022, *MNRAS*, 510, 1223
- Gatti & Sheldon et al., 2021, *MNRAS*, 504, 4312
- Gatti M., et al., 2021, *arXiv e-prints*, p. arXiv:2108.01600
- Gatti M., et al., 2022, *Phys. Rev. D*, 106, 083509
- Gatti M., et al., 2024, *Phys. Rev. D*, 109, 063534
- Gebhardt M., et al., 2023, *arXiv e-prints*, p. arXiv:2307.11832
- Goldstein S., Philcox O. H. E., Hill J. C., Hui L., 2024, *Phys. Rev. D*, 110, 083516
- Goobar A., Leibundgut B., 2011, *Annual Review of Nuclear and Particle Science*, 61, 251
- Gruen D., et al., 2018, *Phys. Rev. D*, 98, 023507
- Handley W. J., Hobson M. P., Lasenby A. N., 2015, *MNRAS*, 450, L61
- Heymans C., et al., 2006, *MNRAS*, 368, 1323
- Heymans C., et al., 2021, *A&A*, 646, A140
- Huff E., Mandelbaum R., 2017, *arXiv e-prints*, p. arXiv:1702.02600

Hunter J. D., 2007, *Computing in Science and Engineering*, 9, 40

Jain B., Seljak U., White S., 1998, *arXiv e-prints*, pp astro-ph/9804238

Jeffrey N., et al., 2025, *MNRAS*, 536, 1303

Kaiser N., Wilson G., Luppino G. A., 2000, *ArXiv Astrophysics e-prints*,

Krause E., Eifler T., 2017, *MNRAS*, 470, 2100

Krause E., et al., 2021, *arXiv e-prints*, p. arXiv:2105.13548

LSST Science Collaboration et al., 2009, *arXiv e-prints*, p. arXiv:0912.0201

Lange J. U., 2023, *MNRAS*, 525, 3181

Lee E., et al., 2022, *MNRAS*, 517, 5303

Li X., et al., 2023, *Phys. Rev. D*, 108, 123518

Lim S. H., Barnes D., Vogelsberger M., Mo H. J., Nelson D., Pillepich A., Dolag K., Marinacci F., 2021, *MNRAS*, 504, 5131

Linder E. V., 2023, *arXiv e-prints*, p. arXiv:2304.04803

Longley E. P., et al., 2023, *MNRAS*, 520, 5016

MacCrann & Becker et al., 2022, *MNRAS*, 509, 3371

Mandelbaum R., 2018, *ARA&A*, 56, 393

McKinney W., 2011, *Python for High Performance and Scientific Computing*, 14

Mead A. J., Heymans C., Lombriser L., Peacock J. A., Steele O. I., Winther H. A., 2016, *MNRAS*, 459, 1468

Mead A. J., Tröster T., Heymans C., Van Waerbeke L., McCarthy I. G., 2020, *A&A*, 641, A130

Mead A. J., Brieden S., Tröster T., Heymans C., 2021, *MNRAS*, 502, 1401

Ménard B., Scranton R., Schmidt S., Morrison C., Jeong D., Budavari T., Rahman M., 2013, *arXiv e-prints*, p. arXiv:1303.4722

Merloni A., et al., 2012, *arXiv e-prints*, p. arXiv:1209.3114

Mortonson M. J., Weinberg D. H., White M., 2013, *arXiv e-prints*, p. arXiv:1401.0046

Muir J., et al., 2020, *Mon. Not. Roy. Astron. Soc.*, 494, 4454

Myles & Alarcon et al., 2021, *MNRAS*, 505, 4249

Olsen K., et al., 2018, *arXiv e-prints*, p. arXiv:1812.02204

Omori Y., et al., 2023, *Phys. Rev. D*, 107, 023529

Pandey S., et al., 2022, *Phys. Rev. D*, 105, 123526

Planck Collaboration et al., 2020a, *A&A*, 641, A1

Planck Collaboration et al., 2020b, *A&A*, 641, A6

Racca G. D., et al., 2016, in MacEwen H. A., Fazio G. G., Lystrup M., Batalha N., Siegler N., Tong E. C., eds, *Society of Photo-Optical Instrumentation Engineers (SPIE) Conference Series Vol. 9904, Space Telescopes and Instrumentation 2016: Optical, Infrared, and Millimeter Wave*. p. 99040O (arXiv:1610.05508, doi:10.1117/12.2230762)

Raveri M., Doux C., 2021, *Phys. Rev. D*, 104, 043504

Samuroff S., et al., 2019, *MNRAS*, 489, 5453

Samuroff S., et al., 2023, *MNRAS*, 524, 2195

Sánchez & Prat et al., 2022, *Phys. Rev. D*, 105, 083529

Sánchez J., et al., 2023a, *MNRAS*, 522, 3163

Sánchez C., et al., 2023b, *MNRAS*, 525, 3896

Schmidt F., 2008, *Phys. Rev. D*, 78, 043002

Schneider P., 2005, *arXiv e-prints*, pp astro-ph/0509252

Schneider A., Teyssier R., 2015, *J. Cosmology Astropart. Phys.*, 2015, 049

Schneider A., Teyssier R., Stadel J., Chisari N. E., Le Brun A. M. C., Amara A., Refregier A., 2019, *J. Cosmology Astropart. Phys.*, 2019, 020

Secco & Samuroff et al., 2022, *Phys. Rev. D*, p. 023515

Secco L. F., et al., 2022, *Phys. Rev. D*, 105, 103537

Shao M., Anbajagane D., 2024, *The Open Journal of Astrophysics*, 7, 29

Shao M. J., Anbajagane D., Chang C., 2023, *MNRAS*, 523, 3258

Sheldon E. S., Huff E. M., 2017, *ApJ*, 841, 24

Shin T., et al., 2019, *MNRAS*, 487, 2900

Spergel D., et al., 2015, *arXiv e-prints*, p. arXiv:1503.03757

Stiskalek R., Bartlett D. J., Desmond H., Anbajagane D., 2022, *MNRAS*, 514, 4026

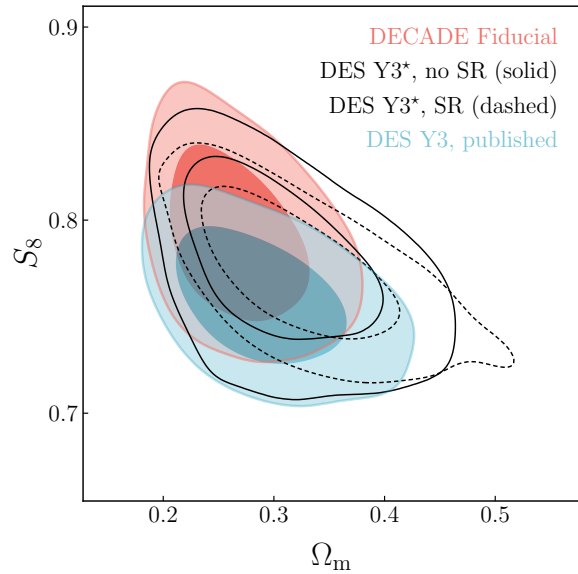


Figure A1. Constraints on Ω_m and S_8 from DECADE and DES Y3. We show three variants of DES Y3. The DES constraints with \star denote results from DES Y3 re-analysed using our inference pipeline. SR stands for the shear ratio measurements (Sánchez & Prat et al. 2022) and is not available in the DECADE data. The constraints from our re-analysis of DES Y3 differ from the published constraints due to a few reasons discussed in Section A, and the contour sizes differ as our analysis pipeline does not include SRs. See text for more details.

Sugiyama S., et al., 2023, *Phys. Rev. D*, 108, 123521

Takahashi R., Sato M., Nishimichi T., Taruya A., Oguri M., 2012, *ApJ*, 761, 152

The LSST Dark Energy Science Collaboration et al., 2018, *arXiv e-prints*, p. arXiv:1809.01669

Thornton R. J., et al., 2016, *ApJS*, 227, 21

Tröster T., et al., 2022, *A&A*, 660, A27

Troxel M. A., et al., 2018, *MNRAS*, 479, 4998

Van der Walt S., Colbert S. C., Varoquaux G., 2011, *Computing in Science and Engineering*, 13, 22

Virtanen P., et al., 2020, *Nature Methods*, 17, 261

Vogelsberger M., Marinacci F., Torrey P., Puchwein E., 2020, *Nature Reviews Physics*, 2, 42

Wagner C., Schmidt F., Chiang C.-T., Komatsu E., 2015, *J. Cosmology Astropart. Phys.*, 2015, 042

Wittman D. M., Tyson J. A., Kirkman D., Dell’Antonio I., Bernstein G., 2000, *Nature*, 405, 143

Yamamoto & Becker et al., 2025, *arXiv e-prints*, p. arXiv:2501.05665

York D. G., et al., 2000, *The Astronomical Journal*, 120, 1579

Zuntz J., et al., 2015, *Astronomy and Computing*, 12, 45

Zürcher D., et al., 2022, *MNRAS*, 511, 2075

de Jong J. T. A., et al., 2015, *A&A*, 582, A62

A RE-ANALYSING DES Y3 WITH THE DECADE PIPELINE

When comparing against — and combining with — the constraints from DES Y3 cosmic shear, we follow the

philosophy of [DES and KiDS Collaborations et al. \(2023\)](#) and reanalyze the DES Y3 data vector with the same inference pipeline used for the DECADE data. The main difference between our pipeline and that of DES Y3 are as follows, in decreasing order of importance: (i) we do not use any shear ratio information (SR, [Sánchez & Prat et al. 2022](#)) as this is not available in DECADE, (ii) we follow [DES and KiDS Collaborations et al. \(2023\)](#) in using the non-linear matter power spectrum model of [Mead et al. \(2020, 2021\)](#) rather than that of [Takahashi et al. \(2012\)](#), and; (iii) we use a slightly narrower prior for the different IA parameters, using $X \in [-4, 4]$ instead of $[-5, 5]$. The difference from (ii) shifts the constraint on S_8 slightly, as documented in [Secco & Samuroff et al. \(2022\)](#) and [DES and KiDS Collaborations et al. \(2023\)](#), while that from (i) widens the posterior width by 1.8 \times , relative to the published result of DES Y3 ([Secco & Samuroff et al. 2022](#); [Amon et al. 2022](#)). This is expected as SRs are known to help constrain IA parameters and self-calibrate redshift uncertainties, thereby improving the constraints on cosmic shear cosmology. This was also noted in [Amon et al. \(2022, see their Figure 15 and Appendix B\)](#). The effect is significant when using the TATT model as the model has 5 free parameters, but is still prominent when using NLA as well. [Figure A1](#) shows the contours for the different variants discussed above. We have verified that we reproduce the published constraints from DES Y3 if we modify our pipeline to match their analysis choices.

B ADDITIONAL PARAMETER CONSTRAINTS

B1 Intrinsic Alignments

The top left panels of [Figure B1](#) show constraints on the IA parameters from DECADE and DES Y3. As discussed previously, the DECADE constraints prefer non-zero values for the IA parameters. These values are consistent with the (broad) posteriors from DES Y3 both when using/discarding the shear ratio measurements (SRs). Though in the former case, there is degraded consistency for the value of a_2 .

The top right panels of the same figure show the behavior of the IA parameters in our joint analysis, including a version where the two datasets share a common set of TATT parameters. We show the DECADE-only and DES Y3-only results for comparison. The combined analysis, when the IA model is not shared, finds similar posteriors to those of the individual surveys. The ‘‘Joint IA’’ result, where the IA model *is* shared, has the same IA posteriors as the DECADE-only result. This is expected as DECADE has a strong preference for non-zero values in a_1, a_2 , with posteriors that are still broadly consistent with those of DES Y3. Thus, the combined analysis moves to the region of parameter space preferred by DECADE since DES Y3 can still accommodate

such values. Interestingly, the p -value of the DES Y3 best-fit changes negligibly (from $p = 0.22$ to $p = 0.23$) between the analyses with independent/joint IA parameters. The same for DECADE changes from $p = 0.02$ to $p = 0.015$. The best-fit for the combined data vector (with scale cuts) corresponds to $p = 0.03$. The final constraints from the ‘‘Joint IA’’ model are,

$$S_8 = 0.775^{+0.021}_{-0.026}, \quad (\text{B1})$$

$$\Omega_m = 0.298^{+0.038}_{-0.049}, \quad (\text{B2})$$

which is consistent with the other lensing constraints discussed in [Section 4](#) above.

Next, the bottom panels of [Figure B1](#) show the IA contours for a few different variant analyses (see [Figure 6](#)). First and foremost, the IA constraints are unchanged even if we drop the three bin-pairs contributing to our poor χ^2 (see [Section 5.1](#)). Thus, those bin-pairs do not drive any specific preference in the IA parameter space. We also show results from dropping different subsets of the data. In all cases, the constraints on a_1 are fairly similar, but those on a_2 change noticeably. In particular, dropping a subset results in a broader posterior that is consistent with $a_2 = 0$.

[Figure B2](#) shows the IA amplitudes a_1, a_2 for the w CDM analysis. There is a somewhat weak correlation between $a_2 - w$, and the negative values of the former, as preferred by the data, can slightly push w to more negative values as well. [Figure B2](#) also shows the constraints from using a shared set of IA parameters for the joint analysis, which are

$$S_8 = 0.725^{+0.019}_{-0.033} \quad (\text{B3})$$

$$\Omega_m = 0.257^{+0.035}_{-0.052} \quad (\text{B4})$$

$$w = -1.61^{+0.37}_{-0.13}. \quad (\text{B5})$$

This constraint on w is consistent with Λ CDM within 1.6σ . The combined constraint is slightly improved, as expected, when using a common set of IA parameters for both datasets.

Next, we address the fact that the posteriors on η_1, η_2 are limited by their prior ranges; note that the same behavior is also found in the DES Y3 cosmic shear analysis ([Secco & Samuroff et al. 2022, see their Figure 17](#)). We run a DECADE variant analysis (‘‘Wide-IA’’) where the prior is significantly wider, $-10 < x_{\text{IA}} < 10$ for all IA parameters, x . In this case, the constraints occupy extreme values, introduce bimodality into the posteriors — and into S_8 as a result — but *do not improve the goodness-of-fit compared to the Fiducial analysis*.

We have identified the cause of the bimodality is solely in a_1, η_1 , as the flexibility in those parameters is being used to force the posteriors of the redshift calibration parameters, Δz_i , to match their prior (see [Figure B3](#)). This matching boosts the posterior probability in the extreme regions of IA parameter space and causes the bimodal constraints. However, the

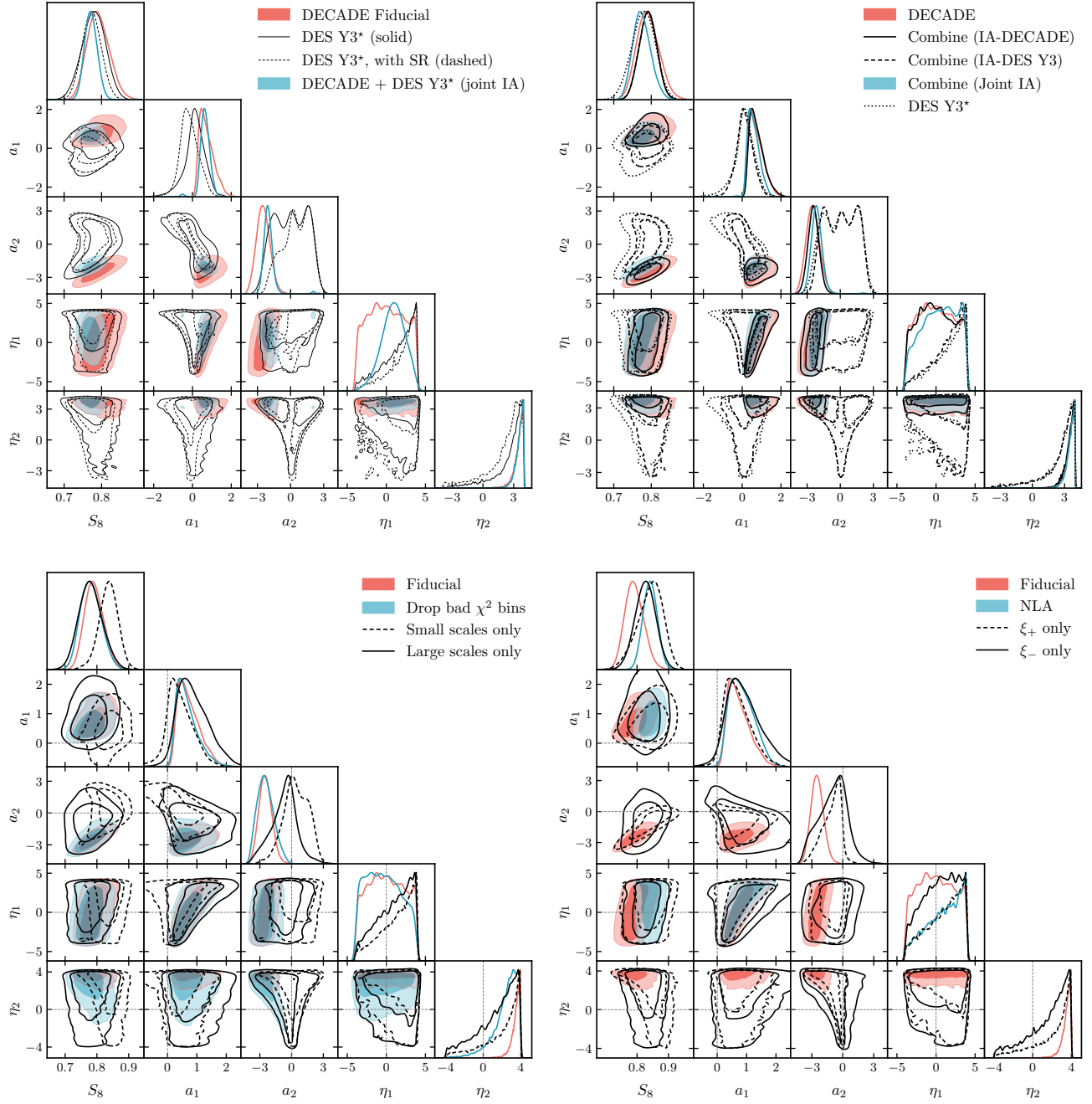


Figure B1. Constraints on the IA parameters for different analysis setups and different datasets, all under the Λ CDM model. **Top Left:** the IA constraints for the results shown in Figure 4. **Top right:** IA constraints for different subsets of the DECADE and DES Y3 analysis. The black solid/dashed lines show the results from the “independent IA” setup where each dataset has its own TATT parameters, while the blue contours show the results from using a common set of parameters for both. **Bottom:** Constraints for different variants of the DECADE analysis. The constraints on a_1 are similar between TATT and NLA — and are also fairly similar if we drop any subset of our data — but those on a_2 broaden significantly and become consistent with $a_2 = 0$ once we drop some subsets of the data. Notably, dropping the three bin-pairs that contribute to our poor χ^2 (see Section 5.1) have IA posteriors that are very similar to those from our Fiducial analysis.

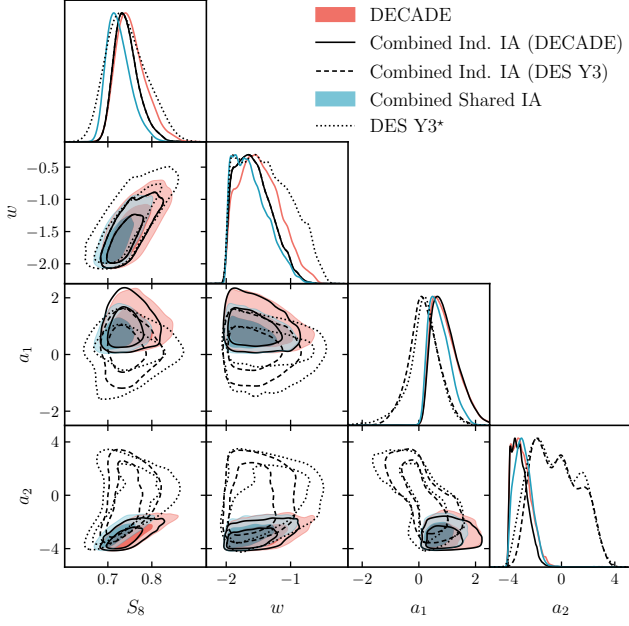


Figure B2. Similar to the top right panel of Figure B1 but for w CDM. There is a mild correlation between $a_2 - w$ for the DECADE IA parameters.

posteriors of Δz_i in our Fiducial constraint are still *consistent with the priors* — the mean value of the posterior is at-most $< 0.8\sigma$ from $\Delta z_i = 0$ — so the extreme values in our Wide-IA analysis are not compensating for any significant bias found in the redshift calibration. We therefore interpret the Wide-IA result as an “overfitting” scenario. Finally, we confirm that widening the priors on only a_2, η_2 causes no bimodality and gives a constraint of $S_8 = 0.786^{+0.027}_{-0.031}$. This mean value *and posterior width* are completely consistent with our Fiducial result. For this reason, we are comfortable using our current IA priors for all cosmological inference.

Under the current priors, the IA posteriors prefer $a_1 > 0$ and $a_2 < 0, \eta_2 > 0$. In Figure B4, we explore the origin of these preferences. We compute best-fit predictions, but now fixing a subset of the IA amplitudes to zero¹⁶ while the rest of the parameters are assigned their values from our Fiducial best-fit constraint. This helps isolate different behaviors in the five-parameter IA model. We first focus on distinguishing between the “linear” terms (green, dependent on a_1) and the “quadratic” terms (purple, dependent on a_2).¹⁷

The value $a_1 > 0$ is preferred as the linear terms (i) reduce power on larger scales for Bins 1 and 2, primarily

¹⁶ Note that $a_1 = 0$ implicitly means $b_{TA} = 0$ as the latter parameter rescales the former for one of the TATT contributions (e.g., Secco & Samuroff et al. 2022, see their Equation 26).

¹⁷ We use the terms “linear” and “quadratic” only heuristically. Our nomenclature is not strictly correct, in particular because a_1 still controls the amplitude of some terms that are quadratic in the density field; see Equations 21-23 in Secco & Samuroff et al. (2022).

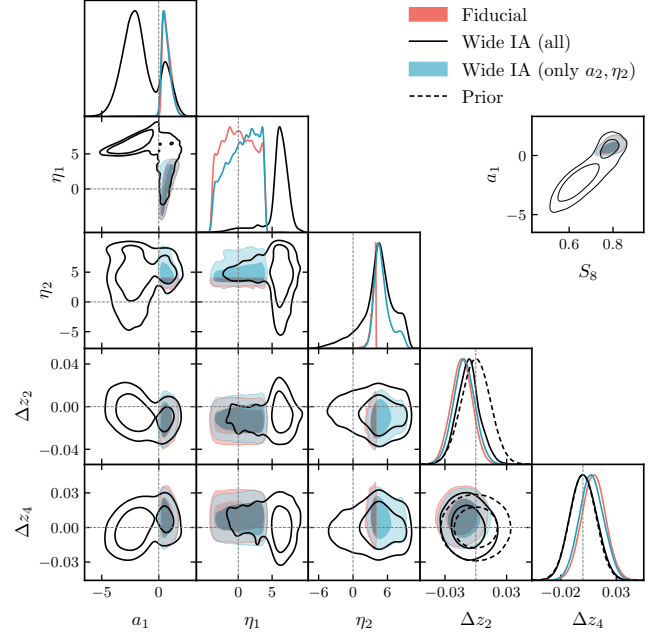


Figure B3. Similar to the top right panel of Figure B1 for different choices of priors on the IA parameters. Setting wide priors of $-10 < x < 10$ on a_2, η_2 alone (blue contour) gives constraints on S_8 that are consistent with the Fiducial analysis. If we set wide priors on all IA parameters (black solid), the model overfits to force the posteriors of Δz_i , the redshift calibration parameters, to agree with their priors (black dashed line). We consider this to be overfitting as the Δz_i posteriors for the Fiducial setup are already consistent with the prior within 0.8σ . The $a_1 - S_8$ plane in the top right shows how the IA bimodality propagates into S_8 . The priors are shown only for Δz_i .

in ξ_+ but somewhat in ξ_- as well, and; (ii) reduce power on all scales in bin pairs (1,4) and (1,3). The auto/cross-correlations with Bin 1 and Bin 2 see the largest effect, which are also the measurements with an inherently lower signal-to-noise. The quadratic term has effectively no contribution on these larger angular scales; particularly in ξ_+ , where it is essentially zero. This is consistent with Figure B1 where the large scales-only analysis prefers $a_2 = 0$. Instead, the main impact from the quadratic contribution is on small-scales, and across all bins. We are unable to isolate which combination of data points induce this overall preference. Note also this term also amplifies ξ_- on smaller scales, but such scales are already removed by our scale cuts (gray bands) and have no impact on our final constraints. This shows that the preference for $a_2 \neq 0$ is predominantly from the higher-signal-to-noise ξ_+ measurement rather than the ξ_- one, as is also found in Figure B1. To summarize, the IA model finds $a_1 > 0, a_2 < 0$ to accommodate a mild scale dependence preferred by the data.¹⁸

¹⁸ We have checked, using simulated data vectors, that catastrophic redshift errors — for example, if our mean redshift is wrong by $\Delta z = 0.1$, which is nearly ten times worse than our calibrated priors — do not generate a scale dependence that mimics the one predicted by the best-fit IA model.

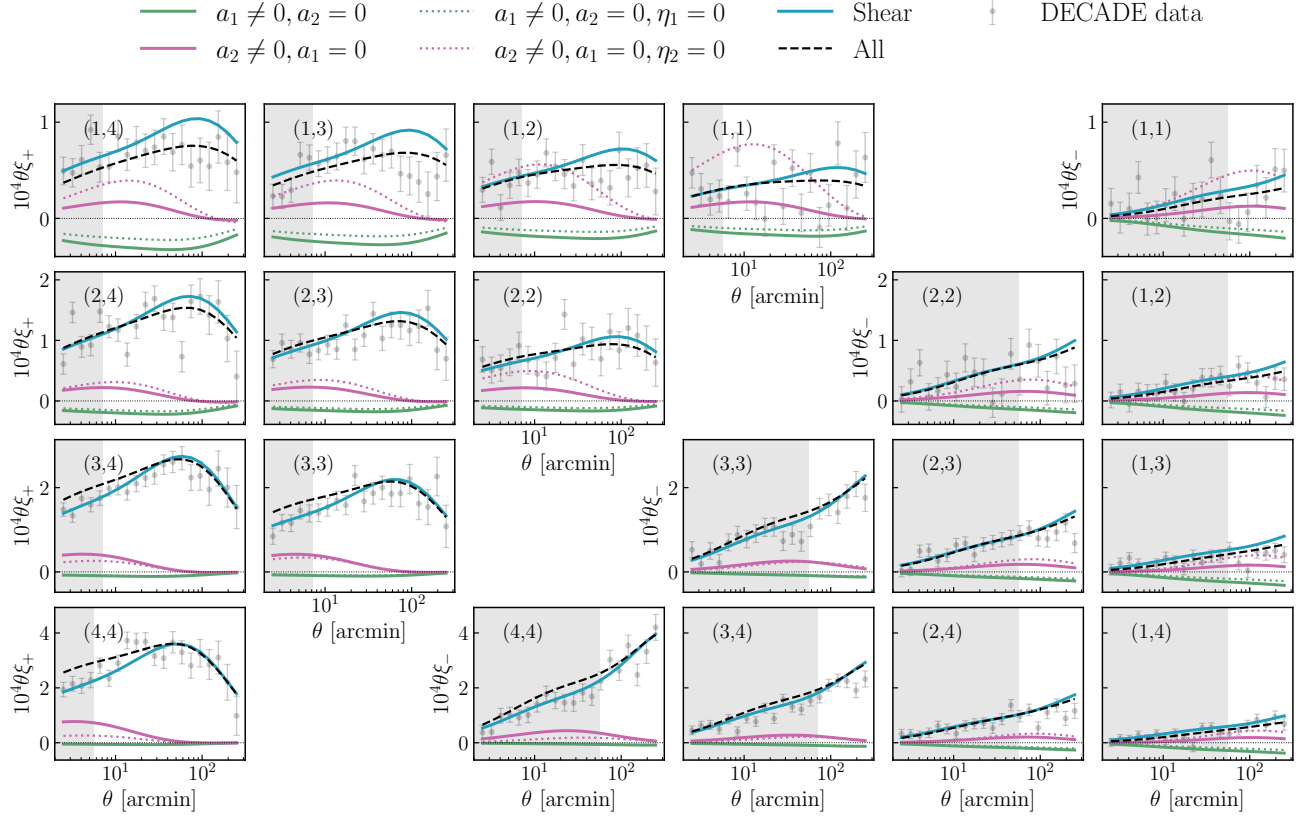


Figure B4. The contributions of different IA parameters to the final ξ_{\pm} best-fit prediction under Λ CDM. We show the IA contributions from nulling out specific amplitudes, and from nulling out only the redshift scaling of a given amplitude (see legend). The fiducial prediction is given as a black, dashed line alongside the DECADE data (gray points). The prediction with no IA contribution is shown as the blue line. For the ξ_+ data vector, the a_1 contribution suppresses power on large-scales and at low redshift, whereas the a_2 contribution amplifies power on small-scales at high redshift. The a_1, a_2 terms cancel their contributions somewhat for the small-scales at lower redshifts. The preference for $\eta_2 > 0$ suppresses the quadratic, a_2 IA terms at low redshift (purple dotted vs. solid), whereas η_1 has negligible impact in comparison. The ξ_- data vector finds similar behavior to ξ_+ but at a somewhat suppressed level. Most notably, it also prefers a slight suppression of power on large-scales. The a_2 contributions are mostly negligible to ξ_- as the former’s impact is on angular scales already discarded by our scale cuts (gray band).

Having identified the need for non-zero amplitudes in the linear/quadratic IA terms, we then check the redshift dependence associated with these amplitudes. We recompute IA contributions but fix the redshift power-law indices, $\eta_1, \eta_2 = 0$. These results are shown as dotted lines. The linear term’s redshift scaling, η_1 , has very little impact given that scaling parameter is mostly unconstrained (Figure B1). However, the same scaling for the quadratic term is found to prefer $\eta_2 > 0$ as mentioned above. Comparing the dashed and solid purple lines in Figure B4 shows that the low-redshift datapoints motivate this preference. Specifically, they prefer a smaller amplitude for the quadratic contribution, and so η_2 must take large values to suppress the relevant amplitude at such redshifts (see Equation 4). While Figure B4 shows that different subsets of the data vector are driving the preference in different IA parameters, we show that re-analyzing our data using/discarding such subsets results in S_8 constraints that are still within 1σ of our Fiducial result (Section 5.3).

In summary, we have undertaken numerous, extensive tests of the IA posteriors to understand the origin of the parameter constraints and check the possibility of systematics driving these constraints. Our tests, the primary of which are the reanalyses of the forty-six catalog-level splits (PAPER III), find consistent results for the IA constraints and do not isolate any particular systematic as a potential cause for the observed behavior. It is therefore still possible that our constraints reflect (at least partly) a real IA signal in the data. It is also remains possible that some part of the constraint is driven by a non-IA contribution that is not probed by our forty-six splits. Regardless, we stress that the S_8 constraints from our numerous IA-related tests are *consistent with our Fiducial results* and highlight the robustness of our quoted constraints. Subsequently, the extensive discussion of IA necessitated in this work further highlights the subtleties in constraining and *understanding* the IA signal in a lensing sample without the use of additional data, *e.g.*, spectroscopic datasets like those

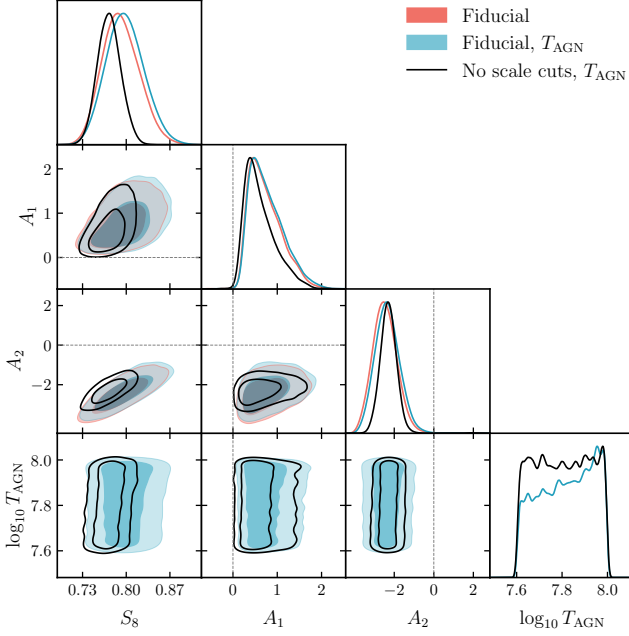


Figure B5. Constraints from DECADE after including baryon corrections in the matter power-spectrum using the model of Mead et al. (2021), and after removing all scale-cuts in addition to the baryon modeling. The parameter T_{AGN} is an effective feedback strength, and higher values correspond to stronger suppression of the power spectrum; see Mead et al. (2021) for more details. The constraints from all analysis choices are consistent, and there is no coupling between the IA and T_{AGN} .

used in Samuroff et al. (2023) or photometric “lens” samples like those used in Samuroff et al. (2019) and Samuroff et al. (2023).

B2 Small-scales and baryons

Our scale cuts are primarily motivated by the uncertainty in the non-linear power spectrum model on small scales. The evolution of structure on these small scales is significantly altered by the non-gravitational processes of baryons; predominantly, this is the ejection of gas outside of the halo due to energetic feedback (Chisari et al. 2018). Hydrodynamical simulations (see Vogelsberger et al. 2020, for a review), which model these effects through approximate “subgrid” prescriptions, generate a variety of predictions for the properties of halos in simulations (e.g., Anbajagane et al. 2020; Lim et al. 2021; Lee et al. 2022; Stiskalek et al. 2022; Anbajagane et al. 2022a,b; Shao et al. 2023; Shao & Anbajagane 2024; Gebhardt et al. 2023) which translates into a variety of predictions for changes in the non-linear matter power spectrum (e.g., Chisari et al. 2018; Amon & Efstathiou 2022). Such variations can be represented through phenomenological, halo-based models such as “Baryonification” (Schneider & Teyssier 2015; Schneider et al.

2019; Aricò et al. 2021; Anbajagane et al. 2024a) and also a variant of the HMCODE2020 model (Mead et al. 2021). The latter includes a T_{AGN} parameter that quantifies the baryonic contribution to the non-linear matter power spectrum, and this parameter was varied in the joint-analysis of DES and KiDS (DES and KiDS Collaborations et al. 2023).

We mimic the setup of the joint-analysis of DES and KiDS, and run two analysis variant where we explicitly model baryon corrections through the T_{AGN} parameter mentioned above. In particular, we run one variant where we use the same scale cuts as the Fiducial analysis and another where we use all available scales in the data vector. In both cases, we use the prior $T_{\text{AGN}} \in [10^{7.6}, 10^{8.0}]$ which is the range the model is calibrated for. The posterior is shown in Figure B5. The T_{AGN} is unconstrained, similar to findings from DES and KiDS Collaborations et al. (2023); Bigwood et al. (2024). Allowing freedom in the T_{AGN} parameter does not change any of the IA amplitudes, and shifts S_8 (relative to the Fiducial constraints) by less than $\approx 0.5\sigma$.

B3 Full parameter space

In Figure B6 we show posteriors from the full parameter space in our fiducial Λ CDM analysis (red) and the prior that we sample from (black). We discuss the behavior of the intrinsic alignment (IA) parameters extensively in Section 5.2 and Appendix B1, so we do not elaborate further in this section.

C UNBLINDING TESTS AND FINDINGS

For this work, we make all the analysis choices (the model, priors, and scale cuts) using simulated data vectors. These relevant tests/analyses are found in PAPER III. Once the analysis choices are fixed, we perform a number of checks on the blinded data vectors (see Section 3 for details on our unblinding method). These tests, together with all the previous tests on the data and the model, cross-check the robustness of our results and justify unblinding the data vector. The full criteria for unblinding is summarized below:

- **Shear catalog tests:** All tests described in PAPER I must pass, which include a number of tests that show the galaxy shape catalog does not contain significant contamination from point-spread function modeling, and does not correlate with image data quality. We also test for B-modes and tangential shear around locations where we do not expect cosmological signals.
- **Redshift tests:** All tests described in PAPER II must pass, which primarily includes a check that the redshift distribution estimated through the SOMPZ method is consistent with that estimated from clustering redshifts.

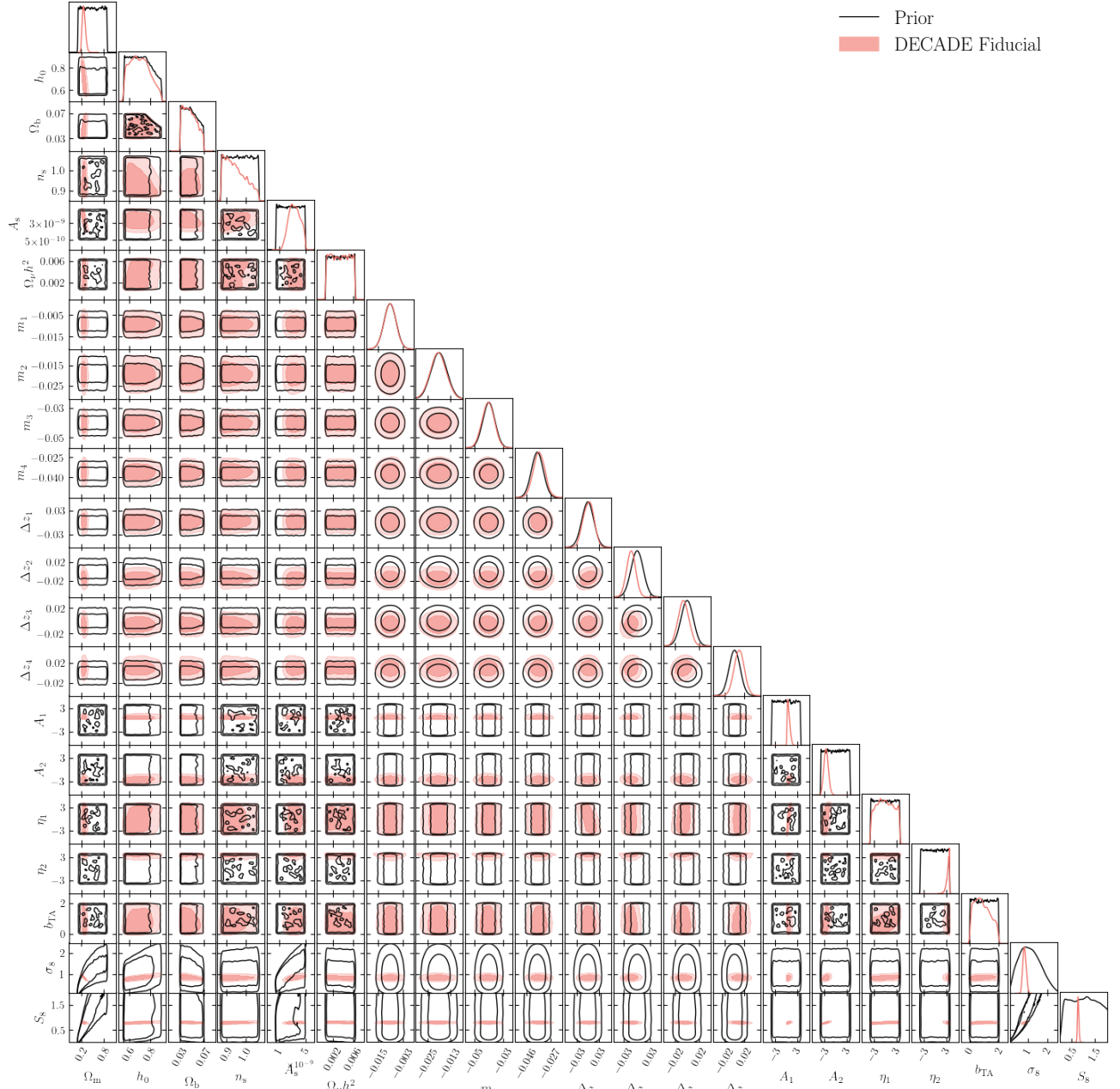


Figure B6. Full parameter constraint for the fiducial analysis (Section 4.1, Figure 4). We also plot the priors associated with this chain.

- **Methodology tests:** All tests described in PAPER III must pass, which includes checking that the cosmological inference pipeline is robust to different analysis choices. We also perform forty-six different end-to-end tests using subsets of the data split by observing conditions or galaxy properties, and check that the resulting cosmological constraints are consistent with our fiducial results. Our criteria was 3σ consistency, but we find all tests pass within 2σ with most passing within 1σ .
- **Final tests (with blinded Λ CDM chains):**
 - We visually inspect the constraints in the full parameter space to see that posteriors on the relevant parameters (*e.g.*, Ω_m , S_8 , a_1 , a_2) are not pushing against the priors in an unexpected way.¹⁹ We also checked that our nuisance parameters, m_i and Δz_i , had posteriors that were consistent with the priors, *i.e.*, the final constraints did not shift to extreme values in the prior.

¹⁹ Some IA parameters, such as η_1 and η_2 are expected to be prior-dominated (Secco & Samuroff et al. 2022; Amon et al. 2022) and were not used in this test. See Appendix B1 for discussions on the chosen prior ranges for these parameters.

- The goodness-of-fit for our best-fit model has a p -value > 0.0015 which corresponds to the model and data being consistent within $< 3\sigma$.
- When comparing constraints on S_8 from the Fiducial analysis, to those obtained by dropping individual redshift bins, the differences in the constraints are less than 3σ .²⁰

We define “parameter shifts/differences” using the simple distance calculation in the S_8 direction, assuming Gaussian posteriors:

$$\text{number of } \sigma = \frac{[S_8]_1 - [S_8]_2}{\sqrt{\sigma([S_8]_1)^2 + \sigma([S_8]_2)^2}}, \quad (\text{C1})$$

where $[S_8]_i$ and $\sigma([S_8]_i)$ are the mean and standard deviation of the posterior for constraint i , and the subscripts, 1 and 2, refer to the two posteriors from which we obtain the value of interest. We note that more complex and rigorous distance/tension metrics exist (*e.g.*, Doux et al. 2021; Raveri & Doux 2021), but since most of the constraining power in cosmic shear lies in the S_8 parameter, and the S_8 constraints are fairly Gaussian, this simple metric is sufficient to capture most of the relevant information (*i.e.*, deciding whether a change in S_8 is significant).

The majority of tests above passed fairly trivially. However, there were two results that still pass our established criteria but subverted our prior expectations; for this reason we record them here. Before unblinding, we performed extensive tests associated with these individual results, and ensured we did not find any known source of lensing systematics that generated them:

- The goodness-of-fit was slightly low (though still passing our criteria), and was lower when using the NLA IA model than the TATT model. We then decided to be conservative and use TATT as our fiducial IA model. We also note that using NLA or TATT resulted in $\approx 1.3\sigma$ shift in cosmological parameters (discussed in Section 5). Post-unblinding, we also used Bayesian evidence ratios to find our data showed a strong preference for the TATT model over NLA.
- We identified that our relatively high χ^2 originates from the ξ_+ measurement in three bin pairs (1, 1), (2, 4), (4, 4). The origin of the high χ^2 is not distinctly isolated in one redshift bin, and the residuals do not show any clear trend with scale. More importantly, we

²⁰ We realized post-unblinding that 3σ is likely too inclusive a threshold for this test given the contours will be fairly correlated. However, we note that in practice all the contours result in shifts less than $\sim 1\sigma$, so our choice of a more conservative threshold did not have an impact on the result of this test. See Figure 6.

verified pre-unblinding that our cosmology constraints are consistent at 0.24σ when including/discarding these three bin pairs. Even after discarding these three bin pairs, switching our IA model from TATT to NLA shifts S_8 to higher values. Given all the above results/checks, we determined the relatively high χ^2 could indeed be caused by statistical fluctuations and did not discard these specific bin pairs.

- Our constraints on IA found a significant, non-zero value of a_2 , which is not unreasonable (*e.g.*, Samuroff et al. 2019) but is somewhat large relative to DES Y3 (Secco & Samuroff et al. 2022; Amon et al. 2022). We used simulated data vectors to find that the presence of noise alone can generate such spurious detection of IA; this is consistent with findings in DES Y3 Amon et al. (2022, see their Figure 15 and Section B). We have since done extensive tests on the interaction of IA with other aspects of our analysis and discuss them extensively in Section 5.2 and Appendix B1.

After unblinding, we regenerated a covariance matrix using the best-fit cosmology from our Fiducial constraint. We then ran chains for our final cosmological constraints, and also re-ran a number of consistency tests to verify that the results did not change. During this process, we discovered one minor/negligible inconsistency in our data pipeline, one in our simulation tests pipeline, and one in our redshift test. We have since corrected them and all final results presented in this series of papers use the corrected versions. None of these changes affect the final constraints from the DECADE dataset. The changes made post-unblinding are

- We discovered a minor inconsistency between the shear weights used in the calculation of m from the image simulations (PAPER I) and the shear weights used in all other applications (*e.g.*, computing effective number densities, data vector computations etc.). This was corrected post-unblinding and the resulting change in m shifted the constraint on S_8 by only 0.08σ . All results presented below (and all tests mentioned above, where relevant) use the post-unblinding, corrected m values.
- We discovered a mismatch in the cosmology used for the simulated data vector and the covariance matrix used in the simulation tests shown in PAPER III. In addition, our simulated data vector was still using the NLA model and was not updated to our fiducial choice of TATT. We have since updated all the simulated data vectors and covariances, and have checked that all tests still pass after the update; all results shown in PAPER III are from the post-correction simulated data vector.
- We improved our redshift test — the χ^2 between the SOMPZ and clustering redshift (WZ) estimates,

shown in Figure 10 of PAPER II — by (i) incorporating uncertainties from the SOMPZ-based redshift samples into the final covariance, (ii) accounting for the free parameters of the SOMPZ-to-WZ forward model in defining N_{dof} for the χ^2 test, and; (iii) limiting the redshift range of the test to $0 < z < 1.6$, as the SOMPZ $n(z)$ has minimal/no support beyond $z > 1.6$. The updated test passes with greater probability than was the case for the pre-unblinding iteration, and the updates above do not affect the fiducial SOMPZ distributions or

the alternative “SOMPZ+WZ” distributions used in this work. See Figure 2, for these $n(z)$ estimates.

This paper was built using the Open Journal of Astrophysics L^AT_EX template. The OJA is a journal which provides fast and easy peer review for new papers in the `astro-ph` section of the arXiv, making the reviewing process simpler for authors and referees alike. Learn more at <http://astro.theoj.org>.